Time-reversal-invariant hexagonal billiards with a point symmetry

T. Araújo Lima,[*] R. B. do Carmo,[†] K. Terto,[‡] and F. M. de Aguiar[§]
Departamento de Física, Universidade Federal de Pernambuco, Recife, PE 50670-901, Brazil

(Received 9 April 2020; revised 3 December 2020; accepted 23 November 2021; published 20 December 2021)

A biparametric family of hexagonal billiards enjoying the C_3 point symmetry is introduced and numerically investigated. First, the relative measure $r(\ell, \theta; t)$ in a reduced phase space was mapped onto the parameter plane $\ell \times \theta$ for discrete time t up to 10^8 and averaged in tens of randomly chosen initial conditions in each billiard. The resulting phase diagram allowed us to identify fully ergodic systems in the set. It is then shown that the absolute value of the position autocorrelation function decays like $|C_q(t)| \sim t^{-\sigma}$, with $0 < \sigma \leqslant 1$ in the hexagons. Following previous examples of irrational triangles, we were able to find billiards for which $\sigma \sim 1$. This is further evidence that, although not chaotic (all Lyapunov exponents are zero), billiards in polygons might exhibit a near strongly mixing dynamics in the ergodic hierarchy. Quantized counterparts with distinct classical properties were also characterized. Spectral properties of singlets and doublets of the quantum billiards were investigated separately well beyond the ground state. As a rule of thumb, for both singlet and doublet sequences, we calculate the first 120 000 energy eigenvalues in a given billiard and compute the nearest neighbor spacing distribution $p(s)$, as well as the cumulative spacing function $I(s) = \int_0^s p(s')\, ds'$, by considering the last 20 000 eigenvalues only. For billiards with $\sigma \sim 1$, we observe the results predicted for chaotic geometries by Leyvraz, Schmit, and Seligman, namely, a Gaussian unitary ensemble behavior in the degenerate subspectrum, in spite of the presence of time-reversal invariance, and a Gaussian orthogonal ensemble behavior in the singlets subset. For $0 < \sigma < 1$, formulas for intermediate quantum statistics have been derived for the doublets following previous works by Brody, Berry and Robnik, and Bastistić and Robnik. Different regimes in a given energy spectrum have been identified through the so-called ergodic parameter $\alpha = t_H/t_C$, the ratio between the Heisenberg time and the classical diffusive-like transport time, which signals the possibility of quantum dynamical localization when $\alpha < 1$. A good quantitative agreement is found between the appropriate formulas with parameters extracted from the classical phase space and the data from the calculated quantum spectra. A rich variety of standing wave patterns and corresponding Poincaré-Husimi representations in a reduced phase space are reported, including those associated with lattice modes, scarring, and high-frequency localization phenomena.

DOI: 10.1103/PhysRevE.104.064211

I. INTRODUCTION

Regular and chaotic motions in classical conservative systems can be quantitatively distinguished through magnitudes associated with the distance between two different trajectories starting from nearby points in the phase space. Such methods of characterization are hampered in quantum mechanics due to Heisenberg's uncertainty principle. Thus, the term *quantum chaos* has been largely used in the literature in the last four decades to encompass major theoretical and conceptual frameworks in the search for genuine quantum mechanical properties that could distinguish the two categories observed in classical Hamiltonian systems. Since the 1970s, it has been recognized that such properties must show up well beyond the ground state of closed quantum systems. A common strategy is to investigate possible correlations of energy eigenvalues and compare the results with predictions of random matrix theory [1]. In order to characterize universality, one must first unfold the energy spectrum, so that a unit mean nearest-neighbor spacing (nns) is obtained. This approach became popular after two important results found by inference: (1) the Berry-Tabor (BT) conjecture [2] and (2) the Bohigas-Giannoni-Schmit (BGS) conjecture [3,4]. The BT conjecture states that, in the semiclassical limit, the statistical properties of the energy spectrum of a classically integrable system must correspond to the prediction of uncorrelated randomly distributed energy levels. As a result, the semiclassical nns distribution $p(s)$ must be Poissonian ($p(s) = e^{-s}$). On the other hand, according to the BGS conjecture, in the case of a classically chaotic system, the spectral properties must follow the universal statistics of the eigenvalues of Gaussian random matrices [1]. If one disregards spin, in the presence or absence of time-reversal symmetry $p(s)$ must correspond to that of the Gaussian Orthogonal Ensemble (GOE) or Gaussian Unitary Ensemble (GUE), respectively.

A convenient way to test predictions of random matrix theory in quantum chaos is to consider a *billiard*. Billiards are prototype models in the ergodic theory of Hamiltonian systems [5]. In a billiard one considers the dynamics of a

[*]tiago.arj@gmail.com
[†]ricardobatistacarmo@gmail.com; Permanent address: Instituto Federal de Alagoas, Piranhas, AL 57460-000, Brazil.
[‡]kaintp@gmail.com
[§]Corresponding author: flavio.aguiar@ufpe.br

particle (unit mass) inside a closed planar domain Ω where it moves freely (unit speed) between specular reflections off the boundary $\partial\Omega$. The phase space of such a system can vary from completely regular to fully chaotic depending on the geometry of $\partial\Omega$. Quantization of a billiard corresponds to solving the Schrödinger (Helmholtz) equation in Ω with Dirichlet boundary condition in $\partial\Omega$. Several numerical methods have been proposed for that purpose in the past decades, so that nowadays one can calculate routinely 100 000 energy eigenvalues for a given $\partial\Omega$.

For classically chaotic systems with time-reversal (TR) invariance and a point-group (PG) symmetry, Leyvraz, Schmit, and Seligman (LSS) [6] have shown that if the TR and the PG operations do not commute, non-self-conjugate-invariant subspaces of the PG must exhibit GUE spectral fluctuations, instead of GOE ones. For example, consider a billiard in the xy plane with the C_3 symmetry. Such a billiard has eigenfunctions ψ_m ($m = -1, 0, +1$), such that ψ_0 is symmetric and repeats itself after a rotation of $2\pi/3$ about the symmetry axis, whereas $\psi_{\pm 1}$ will be repeated only after three consecutive rotations of $2\pi/3$. In other words, if $R(2\pi/3)$ is the rotation operator for an angle of $2\pi/3$, one has $R(2\pi/3)\psi_m = \exp(i\frac{2\pi}{3}m)\psi_m$. Let Θ be the time-reversal operator and H the Hamiltonian with eigenvalue E_m, i.e., $H\psi_m = E_m\psi_m$. Θ is an antiunitary operator that commutes with H. It follows that $H\Theta\psi_m = \Theta H\psi_m = E_m\Theta\psi_m$, i.e., $\Theta\psi_m$ is also an eigenfunction of H with the same eigenvalue E_m. Now, are ψ_m and $\Theta\psi_m$ the same eigenstate? For this subspace one can write $\Theta\psi_m = (-1)^m\psi_{-m}$. Thus, $\Theta\psi_0 = \psi_0$, i.e., ψ_0 is a singlet. On the other hand, ψ_1 and ψ_{-1} must correspond to distinct states. One refers to this doublet state as a Kramers degeneracy. Since these degenerate states are not TR-invariant, they must follow the GUE of random matrices, providing the billiard is classically chaotic, according to the LSS results. Notice that ψ_{-1} is the complex conjugate of ψ_1, so that they have the same C_3-invariant probability distribution ($|\psi_1|^2 = |\psi_{-1}|^2$). In numerical experiments, however, one accesses real linear combinations of ψ_1 and ψ_{-1}, say, φ_1 and φ_2, which are not, in general, C_3-symmetric. In this case, the underlying C_3 symmetry can be observed from the *orthogonal* pair (φ_1, φ_2) through the sum $|\varphi_1|^2 + |\varphi_2|^2$.

While the BT and BGS conjectures have been extensively investigated in the past four decades [7], there has been comparatively scarce studies on the LSS findings. A semiclassical explanation based on periodic orbit theory was reported by Keating and Robbins [8]. Later, microwave and numerical experiments [9–12] addressed the problem, still in chaotic geometries and with a somewhat limited number of eigenvalues. In addition, good statistics were observed for just 2500 eigenvalues in a theoretical model for the electron-phonon interaction in a NEMS coupled to a quantum dot [13]. To our knowledge, little has been said in regard to the situations of (1) fully ergodic but not chaotic classical phase spaces and (2) partially random phase spaces. These gaps are filled here through numerical experiments in a biparametric family of C_3-symmetric hexagonal billiards for which sequences of the first 120 000 singlets and doublets have been calculated separately. For statistical purposes, we disregard the first 100 000 levels, so that only the higher-lying 20 000 eigenvalues are considered in the statistics. The systems studied in this work

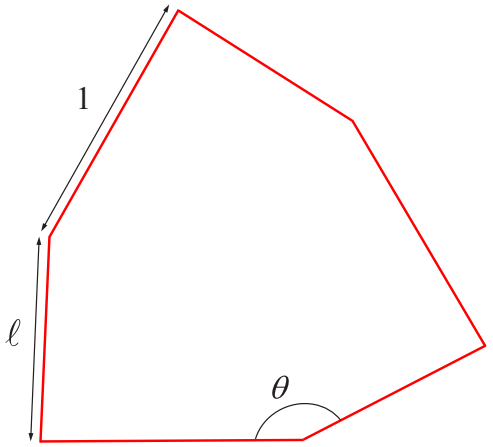

FIG. 1. A C_3-symmetric irregular hexagonal billiard. Alternating adjacent sides with length ℓ and 1, and alternating angles θ and $4\pi/3 - \theta$, define the boundary $\partial\Omega$. The intervals $0 < \ell < 1$ and $\pi/3 < \theta < 2\pi/3$ define the biparametric family.

are described as follows: The polygonal cells are irregular hexagons comprising two alternating adjacent sides, one with fixed unit length, the other one with length ℓ, and two alternating angles, θ and $4\pi/3 - \theta$, as depicted in Fig. 1. Parameters (ℓ, θ) with $0 < \ell < 1$ and $\pi/3 < \theta < 2\pi/3$ define the biparametric family studied here. As $\theta \to \pi/3$, the hexagon approaches an equilateral triangle, regardless of the ℓ value. Also, notice that the intervals $\pi/3 < \theta < 2\pi/3$ and $2\pi/3 < \theta < \pi$ are equivalent. As a reference, we report preliminary results in another C_3-symmetric family of billiards with a smooth $\partial\Omega$. These are similar to the domain studied by LSS, built from an equilateral triangle whose vertices were rounded by two circumferences with radii related through $R = 2r$. We replaced the circumferences by two ellipses with major and minor axes related by $(a_2, b_2) = (2a_1, 2b_1)$. A detailed analysis on this family will be reported separately [14]. Here we refer to a C_3-symmetric billiard with a smooth border in this family as C3S-X, where X = E, if the billiard displays full ergodicity, and X = D, if it exhibits a divided (chaotic and regular regions) phase space.

The paper is organized as follows: Classical properties (relative measure, phase space portraits, position correlation function) of the hexagons are reported in Sec. II. Spectral properties of the quantum counterparts are presented in Sec. III, where we review existing formulas and introduce new intermediate ones for the level spacing distribution between the Poisson and GUE statistics. Fits of histograms of the quantum nns distribution $p(s)$ obtained from the calculated spectra, as well as the computed cumulative spacing function $I(s) = \int_0^s p(s')\,ds'$, are shown to be in good quantitative agreement with the appropriate formulas with parameters extracted from the classical phase space. In Sec. IV a variety of localization phenomena in the hexagonal billiards is presented. As a first step, we briefly discuss the formation of classical periodic orbits (POs) and report the observation of the scarring phenomenon in a number of energy eigenfunctions in the position representation, as well as in the corresponding Poincaré-Husimi function in a reduced phase space. Extended lattice modes are shown to be abundant when

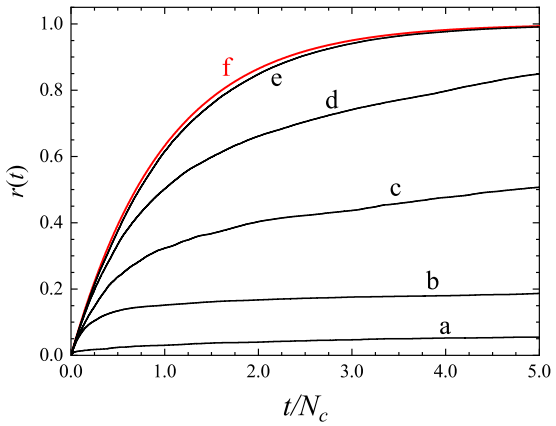

FIG. 2. Solid black lines: Calculated relative measure for billiards in the hexagonal family. The parameter values are $(\ell, \theta) = (0.47, 1.570721)$ in (a), $(0.33, 1.268721)$ in (b), $(0.11, 1.943721)$ in (c), $(0.785, 1.86736)$ in (d), and $(0.94, 2.499721)$ in (e). The solid red (gray, in the printed version) line (f) is the graph of Eq. (1).

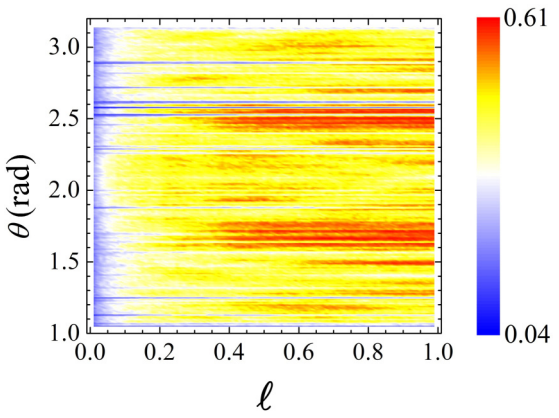

FIG. 3. Calculated phase diagram of the relative measure $r(t = N_c)$ of C_3-symmetric hexagonal billiards, projected onto the $\theta \times \ell$ parameter plane.

θ/π is close to a rational number. In addition, evidence for *focusing* modes (high-frequency localization) in the polygons has also been reported. We close the section with the calculation of the ergodic parameter $\alpha = t_H/t_C$, the ratio between the Heisenberg time and the classical transport time which, for a given billiard, provides an estimate of the distance between the ground-state level and the deep semiclassical regime and, thus, a guide for choosing the appropriate formula of $p(s)$ to fit a given experimental nns distribution. Concluding remarks are presented in the last section.

II. RELATIVE MEASURE, PHASE SPACE, AND DECAY OF CORRELATIONS

In order to characterize the classical dynamics of a given billiard, preliminary calculations were conducted in a Poincaré section. As in previous work on irrational triangles [15], we follow Casati and Prosen [16] by considering collisions of the orbits with a single segment of the all-flat border. In other words, the whole boundary $\partial\Omega$ enters in the dynamics, but we compute the collisions of the particle in one of the segments with unit length. The particle collides off this section at position q and discrete time t, with angle of incidence γ. Let p be the component of the linear momentum parallel to the border. A reduced phase space is then defined by the intervals $0 < q < 1$ and $-1 < p < 1$. For numerical purposes, this rectangle is divided into a large number N_c of cells. Let $n(t)$ be the number of cells visited up to collision t for a given orbit, and $\langle n(t)\rangle$ be its average in a number of randomly chosen initial conditions. The *relative measure* $r(t)$ is defined as the average fraction of visited cells, i.e., $r(t) = \langle n(t)\rangle/N_c$. If all cells have the same probability of being visited, the random model (RM) [17] predicts that $r(t) = r_{\rm RM}(t)$, where

$$r_{\rm RM}(t) = 1 - \exp(-t/N_c). \tag{1}$$

Here we use $N_c = 10^6$ in all numerical experiments. In this case, $r_{\rm RM}(t = 5.0N_c) = 0.993\ldots$. We take this value as a quantifier for a fast trend towards a fully ergodic phase space $[r(t \to \infty) = 1]$. The solid red line in Fig. 2 shows the graph of the function $r_{\rm RM}(t)$. The solid black lines are the calculated $r(t)$ for several hexagons in the family defined in Fig. 1. The closer $r(t)$ is to $r_{\rm RM}(t)$, the better the chance of finding a billiard with the mixing property, according to numerical evidence [15]. In order to look for one such billiard, we calculated $r(t = N_c)$ for a large number (20 000) of members in the family and the result is shown in the phase diagram of Fig. 3. Notice that $r_{\rm RM}(t = N_c) = 0.632\ldots$, so that full ergodicity is displayed earlier by billiards in the red regions in Fig. 3.

Our next step was to look at portraits of the reduced phase space of selected billiards. Two representative results are shown in Fig. 4. The top left panel shows the geometry of $\partial\Omega$ of the billiard with $(\ell, \theta) = (0.94, 2.4997\ldots)$, whose relative measure is shown by curve (e) in Fig. 2, very close to the RM red line (f). The bottom left panel in Fig. 4 shows a portrait of the reduced phase space of this billiard, numerically obtained from a single time series with 10^6 points. In contrast, the billiard with $(\ell, \theta) = (0.47, 1.5707\ldots)$ (top right panel in Fig. 4) displays a reduced phase space (bottom right panel in Fig. 4) comprising six horizontal strips for each sign of p from two different time series (red symbols for one trajectory, black symbols for the other one). These results reflect the fact that for a generic polygonal billiard, the motion in phase space does not occur in a torus, but in multiply handled spheres [18]. Actually, the widths and positions of the strips depend on the initial conditions and the length of the time series. In the top panel of Fig. 5 we show the calculated reduced phase space in the same billiard with $(\ell, \theta) = (0.47, 1.5707\ldots)$, for 10^3 different time series, all with the same length of 10^3 points. Clearly this billiard is ergodic, but, for a single time series, the reduced phase space is swept at a much slower pace. Henceforth, we refer to the billiard with $(\ell, \theta) = (0.94, 2.4997\ldots)$ as the *fast hexagonal billiard* (FHB) and to the $(\ell, \theta) = (0.47, 1.5707\ldots)$ domain as the *slow hexagonal billiard* (SHB). Notice that the ratio θ/π is, to numerical precision, irrational in both hexagonal billiards. The calculated genus is on the order 10^{17} in both cases. In particular, for the domain with $\ell = 0.47$, $\theta/\pi = 0.4999\ldots$. The proximity of θ to the right angle in the SHB is a key ingredient for the rich set of classical and quantum properties observed in this geometry, as discussed in the next sections. For comparison, the bottom panel in Fig. 5 shows the situation in the C3S-D billiard with

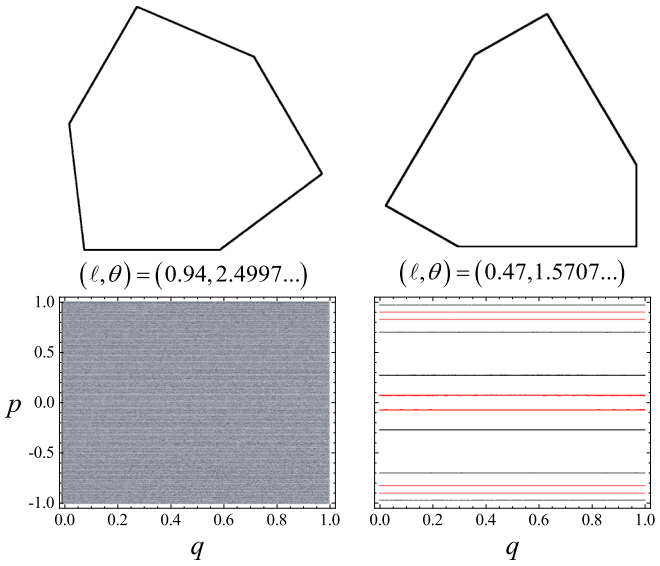

FIG. 4. Bottom panels: Reduced phase space of the C_3-symmetric billiards in the hexagonal family shown in the top panels. On the left, the phase space is built from a single time series. On the right, two different sets of initial conditions were used, corresponding to the black and red (gray, in the printed version) symbols. The hexagon with $(\ell, \theta) = (0.94, 2.4997\ldots)$ quickly displays full ergodicity, as well as a fast decay of correlations (see Fig. 6). It is here referred to as the fast hexagonal billiard (FHB). Convergence and decay of correlations in the hexagon with $(\ell, \theta) = (0.47, 1.5707\ldots)$ are rather sluggish, and we refer to this billiard as the slow hexagonal billiard (SHB).

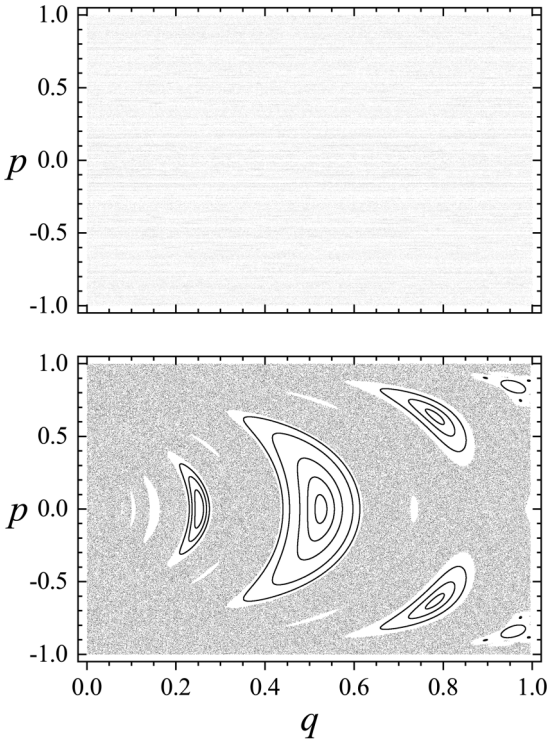

FIG. 5. Top panel: Fully ergodic reduced phase space of the SHB, calculated from a set of 1000 different time series with randomly chosen initial conditions, each one with length $\Delta t = 1000$. Bottom panel: Divided reduced phase space of a C_3-symmetric domain (C3S-D) with a smooth border, as described in the text.

$(a_1, b_1) = (0.288609, 0.281522)$ (see insets in Fig. 10 below), where periodic orbits surrounding elliptical centers as well as chaotic regions are clearly visible.

For a better characterization of the classical dynamics, we also calculated the time averaged position autocorrelation function

$$C_q(t) = \lim_{T\to\infty} \frac{1}{T} \sum_{\tau=0}^{T-1} q(\tau)q(\tau + t) \qquad (2)$$

in the hexagonal billiards. As is well established [5], when chaos is strong, the correlations decay exponentially in time. These concepts have been applied to both dispersing and focusing billiards but, to our knowledge, little has been said in regard to polygonal billiards. While billiards in polygons may be ergodic, all their Lyapunov exponents are zero. Thus, rigorously, their possible random behavior cannot be deemed as a signature of chaos (*Kolmogorov mixing*). However, previous numerical experiments on irrational triangles [15,16] have shown evidence that they might be *mixing*, a category hierarchically below the chaotic one (all chaotic systems are mixing, but not the other way around). This evidence is based on the observation that in certain geometries the correlation functions decay polynomially, sometimes as fast as those in strongly mixing systems, i.e., $|C_q(t)| \sim t^{-\sigma}$, with $\sigma \sim 1$. The solid black lines in Fig. 6 show results for the position autocorrelation function in the two representative hexagons discussed above. Clearly the FHB exhibits a strong mixing character, as indicated by the solid red line, a fit with $\sigma = 1$, in the left panel in Fig. 6. In contrast, the right panel shows a much slower decay of the position autocorrelation function in the SHB, with $\sigma = 0.35$. Guided by these classical features, our next step was to investigate the quantum properties of selected hexagons.

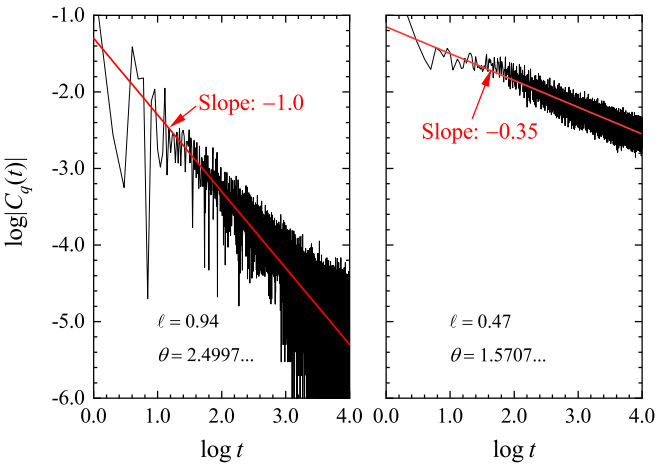

FIG. 6. Left panel: Solid black line: Decadic log-log plot of the calculated position correlation function in the FHB. Solid red (gray, in the printed version) line: Linear fit with a slope of −1.0. This fast decay of the autocorrelation function is an evidence that this billiard enjoys a near strong mixing property. Right panel: The same for the SHB. The linear fit [red (gray, in the printed version) line] has a slope of −0.35.

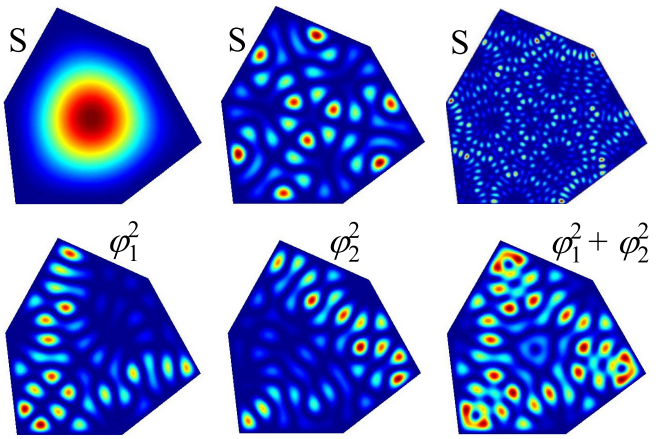

FIG. 7. Top panels: Density plots of squared eigenfunctions corresponding to singlet states in the FHB, exhibiting the underlying C_3 symmetry. Bottom panels: The same for a numerically calculated doublet state (φ_1, φ_2) in the same billiard (left and middle panels). The C_3 symmetry shows up in the sum $\varphi_1^2 + \varphi_2^2$ (right panel), as discussed in the text.

III. QUANTUM PROPERTIES

Quantum billiards are two-dimensional infinite potential wells. The particle is free within domain Ω and cannot be found at the boundary $\partial\Omega$. The time-independent Schrödinger equation leads to the eigenvalue problem of the two-dimensional Laplacian, described by the Helmholtz equation. In other words, in the position representation, the particle's wave function is a solution of

$$\nabla^2\varphi(\vec{r}) = -k^2\varphi(\vec{r}) \tag{3}$$

in Ω, with Dirichlet boundary condition $\varphi(\vec{r}) = 0$ in $\partial\Omega$. Here $k^2 = 2\mu E/\hbar^2$, where μ is the mass of the confined particle, $\hbar = h/2\pi$, h is Planck's constant, and E is the energy eigenvalue. Exact solutions to this problem are known only in a handful of geometries, and one has to rely most often on numerical techniques. As we will describe below, the finite element method (FEM) [19] and the boundary method due to Vergini and Saraceno (VS) [20] are the techniques used here.

A. Low-lying spectra

The FEM is a standard numerical technique in which an arbitrary domain Ω is discretized into very small triangular tiles which form a mesh. In the process, $\partial\Omega$ is actually replaced by a polygonal border with a very large number of small straight segments. The unknown solution is then linearized in each triangular element and the continuity of the wave function at the interfaces of neighboring elements and the boundary condition at $\partial\Omega$ replace the partial differential equation by a computational task of matrix diagonalization for the numerous coefficients. Thus, the method is admittedly memory hungry and has a relatively limited precision. Nevertheless, it is particularly useful in comparison with physical experiments [19] and provides a convenient way to obtain low-lying energy eigenvalues and eigenfunctions through a commercial software such as Matlab. The top panels in Fig. 7 show density plots of three different singlet states in the FHB, all standing wave patterns exhibiting the C_3 symmetry, as expected. The bottom panels in Fig. 7 show a doublet formed by an orthogonal pair, say, (φ_1, φ_2), in the same billiard. As these modes are orthogonal, the sum $\varphi_1^2 + \varphi_2^2$ exhibits the C_3 symmetry (rightmost bottom panel in Fig. 7). The FEM also provides a way to crosscheck the results of the more efficient boundary method.

B. High-lying spectra

For a large sequence of consecutive energy eigenvalues, boundary methods are the numerical techniques of choice. Briefly putting it, in a boundary method one usually expands the unknown solution in terms of basis functions in an outer domain from which $\partial\Omega$ is a subset. The solutions in Ω are unique and, thus, they must correspond to the superpositions which vanish in $\partial\Omega$. Precision is determined by the number N_B of basis functions used in the expansion. The ingenious method of VS [20] is based on the idea of seeking a minimum of the so called *boundary norm*, defined as the path integral over $\partial\Omega$ of $\varphi^2[(k/k_0)\vec{r}]/r_n$, where $\vec{r}$ is the position vector of a point in $\partial\Omega$, $r_n = \hat{n}\cdot\vec{r}$, $\hat{n}$ is the outgoing unit vector normal to $\partial\Omega$ at point $\vec{r}$ and $\varphi(\vec{r})$ is an eigenfunction of the Laplacian with eigenvalue $-k_0^2$. $\varphi[(k/k_0)\vec{r}]$ is assumed to be the Laplacian eigenfunction with eigenvalue $-k^2$. The minimum condition for the boundary norm leads to a generalized eigenvalue problem whose numerical solution provides quantized values k_j, if any, within a small interval $[k_0 - \Delta k, k_0 + \Delta k]$, as well as the N_B coefficients for the truncated expansion of the scaling function $\varphi[(k/k_0)\vec{r}]$ in terms of a proper set of basis functions. That number is estimated to depend on k_0 as $N \simeq 0.9k_0 + 20$ [20]. The interval width $2\Delta k$ is determined by the desired accuracy, since the errors grow as $|k_j - k_0|^3$ [21]. Here we chose a set of C_3-symmetric basis functions for the singlets and a nonsymmetric one for the doublets. Convergence to the semiclassical regime was tested systematically until a small difference was found in the statistics of the first 20 000 levels above the first N_0 ones. In practice, we observe that the rate of convergence depends on $\partial\Omega$, so that our common choice was $N_0 = 100\,000$, which seemed satisfactory in the FHB. On the other hand, we anticipate that this choice was not far enough to reach the deep semiclassical regime in the SHB. We will return to this point in the context of quantum localization in Sec. IV.

C. Level statistics: GOE and GUE

Let us briefly restate the problem that motivated this work. Is there a billiard in our nonchaotic family which might follow the LSS results predicted for chaotic domains [6]? If so, the nns distribution for singlets must be close to

$$p_{\mathrm{GOE}}(s) = \frac{\pi}{2}s\exp\left(-\frac{\pi}{4}s^2\right), \tag{4}$$

which predicts a linear level repulsion $[p(s \to 0) \sim s]$ and is often associated with the energy spectrum of a time-reversal-invariant classically chaotic system. In this case, the cumulative spacing function $I(s) = \int_0^s p(s')\,ds'$ is given by

$$I_{\mathrm{GOE}}(s) = 1 - \exp\left(-\frac{\pi}{4}s^2\right). \tag{5}$$

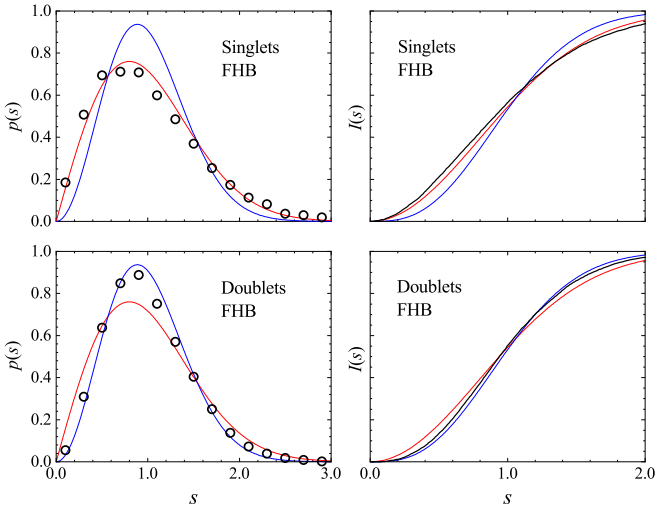

FIG. 8. Symbols: Calculated nns distributions $p(s)$ in the FHB. The graphs on the left show a good agreement of the calculated probability density with the GOE result [solid red (light gray, in the printed version) line] for singlets (top panel) and with the GUE prediction [solid blue (dark gray, in the printed version) line] for doublets (bottom panel). The same agreement is observed through the corresponding cumulative spacing functions $I(s)$ in the right panels [red (light gray, in the printed version) lines for GOE, blue (dark gray, in the printed version) lines for GUE, and black lines for the calculated data in the FHB].

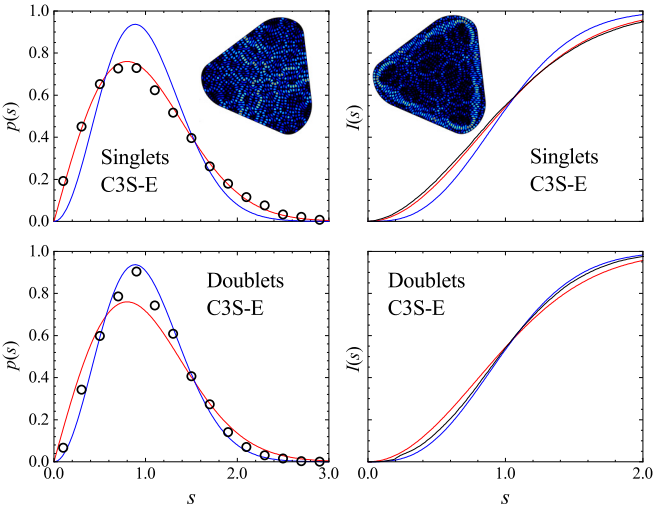

FIG. 9. The same as Fig. 8 for the C3S-E billiard. Insets: Density plot of $|\varphi|^2$ corresponding to extended (left) and whispering gallery mode (right) singlet states in the C3S-E billiard.

On the other hand, when the time-reversal symmetry is broken in the classically chaotic system, the spacing must be distributed according to the GUE of random matrices, for which

$$p_{\mathrm{GUE}}(s) = \frac{32}{\pi^2} s^2 \exp\left(-\frac{4}{\pi} s^2\right), \tag{6}$$

which predicts, instead, a quadratic level repulsion, and for which

$$I_{\mathrm{GUE}}(s) = \mathrm{erf}\left(\frac{2s}{\sqrt{\pi}}\right) - \frac{4}{\pi} s \exp\left(-\frac{4}{\pi} s^2\right). \tag{7}$$

The anomalous result predicted by LSS for a C_3-symmetric TR-invariant classically chaotic billiard is right here: the Kramers doublets must follow the prediction of the GUE, not GOE, despite the presence of the TR symmetry.

From the classical properties of the hexagons, a good candidate to follow the LSS conjecture is the FHB, which seems to enjoy the strong mixing property. Indeed, as shown by the symbols in the left panels in Fig. 8, the high-lying energy eigenvalues in this hexagonal billiard display a spacing distribution $p(s)$ which is very close to the GOE result (solid red line) for singlets and to the GUE result (solid blue line) for doublets. The right panels in Fig. 8 confirm this trend through the cumulative spacing function $I(s)$. For comparison, we repeated the numerical experiments in a smooth billiard. We show in Fig. 9 results for the C3S-E billiard with $a_1 = b_1 = \sqrt{3}/12$, which corresponds to the billiard investigated by LSS [6]. Clearly, we confirm the LSS results for both singlets and doublets. The insets in Fig. 9 show density plots of $|\varphi|^2$ corresponding to singlet states of the LSS billiard, an extended mode on the left and a whispering gallery mode on the right.

D. Level statistics: Poisson-GOE and Poisson-GUE transitions

Now, what if the billiard exhibits a slow decay of classical correlations, such as the SHB, or if the reduced phase space is divided, such as in the C3S-D? The problem of whether a symmetry transition or a transition between integrability and chaos in a given physical system could be described by a transition between Gaussian ensembles or between a Gaussian ensemble and a Poissonian one is not new. In fact, several interpolation formulas have been proposed in the literature in the past few decades [22–25]. Here we follow two approaches. In the first one, we consider the phenomenological formula proposed by Brody [22] for the transition between the Poisson and GOE distributions,

$$p_{\mathrm{B},1}(s) = (\nu+1) a_\nu s^\nu \exp(-a_\nu s^{\nu+1}), \tag{8}$$

where

$$a_\nu = \left[\Gamma\left(\frac{\nu+2}{\nu+1}\right)\right]^{\nu+1}, \tag{9}$$

$\Gamma(x)$ is Euler's gamma function, and $0 \leqslant \nu \leqslant 1$. As demonstrated by Batistić, Lozej, and Robnik [26], the Brody parameter ν can be regarded as a measure of the degree of localization of *chaotic* eigenstates in the phase space (Poincaré-Husimi representations). By following the same steps which led to the Eq. (8), we derived a Brody-like formula for the transition between the Poisson and GUE distributions,

$$p_{\mathrm{B},2}(s) = (\eta+1) b_\eta^2 s^{2\eta} \exp(-b_\eta s^{\eta+1}), \tag{10}$$

where

$$b_\eta = \left[\Gamma\left(\frac{2\eta+1}{\eta+1}\right)\right]^{-(\eta+1)}, \tag{11}$$

and $0 \leqslant \eta \leqslant 1$. For $\eta = 0$, $p_{\mathrm{B},2}(s)$ reduces to the Poisson distribution, whereas for $\eta = 1$ the Wigner distribution for the GUE is obtained.

We also follow the elegant approach of Berry and Robnik (BR) [23] and later developed by Prosen, Batistić, Lozej, and Robnik [26–30]. In this framework, a generic mixed classical dynamics is considered and the corresponding quantum level spacing distribution is derived for different regimes of coupling between the underlying regular and chaotic regions of the phase space. The spectrum is assumed to be a superposition of M statistically independent sequences of levels with level densities ρ_i ($i = 1, \ldots, M$). In particular, if there is only one regular (Poissonian) with level density ρ_1 and one chaotic (GOE) component with $\rho_2 = 1 - \rho_1$, the BR formula reads

$$p_{\mathrm{BR},1}(s) = \left[\left(2\rho_1\rho_2 + \frac{\pi\rho_2^3 s}{2}\right)e^{-\frac{\pi\rho_2^2 s^2}{4}} + \rho_1^2 \mathrm{erfc}\left(\frac{\sqrt{\pi}\rho_2 s}{2}\right)\right] \times e^{-\rho_1 s}, \tag{12}$$

where $\mathrm{erfc}(x)$ is the complementary error function. For $\rho_1 = 0$ ($\rho_1 = 1$), $p_{\mathrm{BR},1}(s)$ reduces to the GOE (Poisson) distribution. By following the steps described in [23], we derived the formula which interpolates the Poisson and GUE distributions, which can be written as

$$p_{\mathrm{BR},2}(s) = \left\{\left[\rho_1^2 + \frac{8}{\pi}\rho_2^2 s\left(\rho_1 + \frac{4}{\pi}\rho_2^2 s\right)\right]e^{-\frac{4}{\pi}\rho_2^2 s^2} + \rho_1\rho_2(2 - \rho_1 s)\mathrm{erfc}\left(\frac{2\rho_2 s}{\sqrt{\pi}}\right)\right\}e^{-\rho_1 s}, \tag{13}$$

so that for $\rho_1 = 0$ ($\rho_1 = 1$), $p_{\mathrm{BR},2}(s)$ reduces to the GUE (Poisson) distribution. It is worth noting that the BR formulas are expected to provide a good description of the deep semiclassical regime. For instance, excellent agreement has been found with numerical experiments in a billiard for which the first 587 654 eigenvalues above the first 1 000 000 ones have been used in the analysis [29]. These are quite impressive numbers. In fact, most of the attempts to fit our data with the BR formulas resulted in poor agreement. This could be an indication that our sets of 20 000 eigenvalues above the first 100 000 ones might still not correspond to a truly semiclassical regime. On the other hand, much better results could be found here with the semiempirical model of Batistić and Robnik [28–30], which takes into account the dynamical localization of chaotic eigenstates and their coupling with the regular ones through tunneling effects. A key result of the theory is the so-called Berry-Robnik-Brody (BRB) distribution, which can be written as

$$p_{\mathrm{BRB},1}(s) = \left\{\frac{\rho_1^2}{(\beta+1)\Gamma\left(\frac{\beta+2}{\beta+1}\right)}Q\left[\frac{1}{\beta+1}; a_\beta(\rho_2 s)^{\beta+1}\right] + \left[2\rho_1\rho_2 + (\beta+1)a_\beta\rho_2^{\beta+2}s^\beta\right]e^{-a_\beta(\rho_2 s)^{\beta+1}}\right\}e^{-\rho_1 s}, \tag{14}$$

for the crossover between the Poisson and GOE distributions. Here a_β is defined in Eq. (9) and $Q(\kappa; x)$ is the incomplete Gamma function. Notice that $p_{\mathrm{BRB},1}(s)$ reduces to the Poisson distribution if $\rho_1 = 1$ or if $\beta = 0$. On the other hand, $p_{\mathrm{BRB},1}(s) = p_{\mathrm{B},1}(s)$ for $\rho_1 = 0$, and $p_{\mathrm{BRB},1}(s) = p_{\mathrm{BR},1}(s)$ if $\beta = 1$. Now, following Batistić and Robnik [28] we derived a formula that corresponds to the Poisson ↔ GUE crossover,

$$p_{\mathrm{BRB},2}(s) = \left\{\rho_1\rho_2 b_\gamma^{\frac{1}{\gamma+1}}(2 - \rho_1 s)Q\left[\frac{1+2\gamma}{1+\gamma}; b_\gamma(\rho_2 s)^{\gamma+1}\right] + \left[\rho_1^2\left(1 + b_\gamma\rho_2^{\gamma+1}s^{\gamma+1}\right) + (1+\gamma)\left(\rho_2^{\gamma+1}b_\gamma s^\gamma\right)^2\right]e^{-b_\gamma(\rho_2 s)^{\gamma+1}}\right\}e^{-\rho_1 s}, \tag{15}$$

where b_γ is defined in Eq. (11). Here $p_{\mathrm{BRB},2}(s) = e^{-s}$ if $\rho_1 = 1$ or if $\gamma = 0$. In addition, $p_{\mathrm{BRB},2}(s) = p_{\mathrm{B},2}(s)$ if $\rho_1 = 0$, and $p_{\mathrm{BRB},2}(s) = p_{\mathrm{BR},2}(s)$ if $\gamma = 1$.

We tested some of the above formulas in two distinct geometries, namely, the SHB and the C3S-D. As discussed above, the SHB combines a fully ergodic phase space with a slow decay of classical correlations. This recipe in irrational triangles yields intermediary quantum spectral statistics, as evidenced by numerical experiments [15]. Since $\rho_2 = 1$ in this domain, the only possibility here is to fit our data with the $p_B(s)$ formulas. The symbols in the left panels in Fig. 10 are results of numerical experiments in the SHB, which clearly depart from the GOE and GUE distributions represented by the red and blue lines, as before. The solid black line is a fit of the data with $p_{\mathrm{B},1}(s)$ with parameter $\nu = 0.7899$ in the top left panel and with $p_{\mathrm{B},2}(s)$ with parameter $\eta = 0.73668$, in the bottom left panel. On the other hand, the C3S-D billiard studied here holds a divided phase space (see Fig. 5) with a fraction $\rho_2 = 0.8$ directly obtained from the calculated relative measure. In this case, the BR and BRB formulas might be used. Since this is still an ongoing work (no attempt has been made thus far to characterize the deep semiclassical regime in the C3S family), here we deliberately focused in lower energy levels of the C3S-D only, in order to test the BRB relations. Specifically, we consider a sequence of 10 000 eigenvalues above the first 10 000 ones. The circles in the right panels in Fig. 10 are the resulting nns distributions from the calculated singlets and doublets spectra. The solid black lines are fits with $p_{\mathrm{BRB},1}(s)$ (top right panel) and $p_{\mathrm{BRB},2}(s)$ (bottom right panel) with the parameter ρ_2 fixed at the experimental value 0.8 and with $\beta = 0.106$, in $p_{\mathrm{BRB},1}(s)$ and $\gamma = 0.527$, in $p_{\mathrm{BRB},2}(s)$. Notice that the singlets spacings are already almost distributed according to the Poisson function, represented in the right panels in Fig. 10 by the solid green lines. The good agreement between the calculated nns distributions of both singlets and doublets and the BRB formulas with the ρ_2 value extracted from the numerically calculated relative measure confirms our expectation that the deep semiclassical regime of the C3S-D billiard is beyond the investigated window of the energy spectrum. The inset in Fig. 10 shows a density plot of $|\varphi|^2$ in the C3S-D billiard corresponding to a *focusing mode* or, in other words, a high-frequency localization. In the next section, we discuss this and other aspects of localization in the FHB and the SHB.

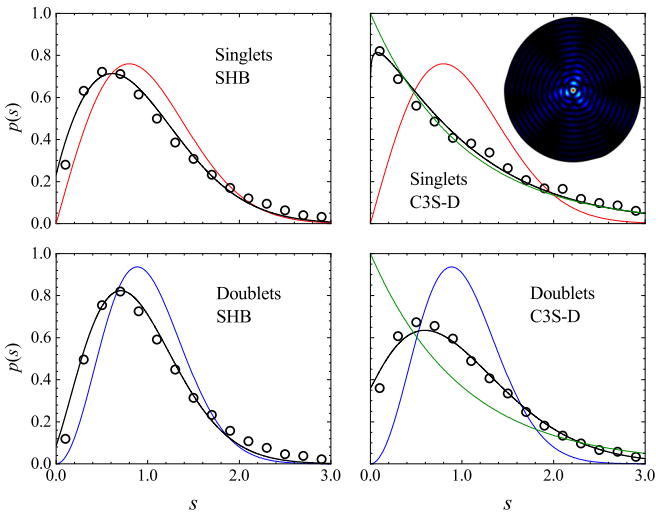

FIG. 10. Open symbols: Calculated nns distributions in the SHB (C3S-D billiard) for singlets in the top left (top right) panel and doublets in the bottom left (bottom right) panel. Solid black lines are fits with $p_{B,1}(s)$ (top left), $p_{B,2}(s)$ (bottom left), $p_{BRB,1}(s)$ (top right) and $p_{BRB,2}(s)$ (bottom right). Parameters are given in the text. Solid red (top panels) and blue (bottom panels) lines are the GOE and GUE distributions, respectively. The solid green line in the right panels is the Poisson distribution, exp(-s). The inset shows a density plot of $|\varphi|^2$ corresponding to a *focusing mode* in the C3S-D billiard with a pronounced peak at the billiard center.

IV. QUANTUM LOCALIZATION

In the quantum description of a particle, if, for a given potential, there is a pronounced enhancement in the probability density $|\varphi(\vec{r})|^2$ in some region of the space swept by $\vec{r}$, or if the momentum distribution $f(p)$ has a peak at $p = 0$ with walls that decay exponentially, one says there is *localization* [31–34]. For a classically ergodic system in the deep semiclassical regime, localizations might not disappear, although their support (effective area) would have zero measure (for a recent discussion on the subject, see Ref. [35]). In the context of quantum billiards, sticking effects near classical phase space structures and the dynamical suppression of diffusive-like motion by quantum interference (dynamical localization) are of particular interest. Noteworthy is the enhancement of quantum probability densities around classical unstable periodic orbits, a phenomenon known as *scarring* in energy eigenfunctions [36], not to be confused with the dynamical localization [29,30,37]. The latter allows one to estimate adequate spectral conditions for a reliable comparison between experiments and predictions by random matrix theory. Billiards in polygons may also exhibit the so-called *super-scarring* property, i.e., persistent structures in high-lying energy eigenfunctions which are not associated with a single unstable periodic orbit, but with families of classical periodic orbits. Originally studied in pseudointegrable billiard models and in the barrier billiard [38,39], superscars are believed to exist in general plane polygonal billiards since (1) the geometry might support the formation of classical channels of parallel periodic orbits and (2) *strong diffraction* might occur at the corners. These are essentially the two mechanisms for the formation of superscars, an interesting subject which was not explored here. In this section, we report results which portray a variety of patterns of energy eigenfunctions in the position representation, $\varphi(\vec{r})$, in the hexagonal billiards, as well as their corresponding Poincaré-Husimi representations $h_k(q, p)$ in a phase space with Birkhoff variables (q, p). Besides scarred eigenfunctions, our findings include extended *lattice* modes and standing wave patterns localized at the geometric center of the hexagon, bearing resemblance to *focusing* modes in billiards with a smooth border, a phenomenon known as *high-frequency localization*. In addition, through the ratio between the Heisenberg and the classical transport times, we estimate the spectral distance between the ground-state and the deep semiclassical regime in the FHB and SHB. First, we discuss possible classical periodic orbits in the hexagonal geometry.

A. Periodic orbits and scarring in the rational hexagon with $(\ell, \theta) = (0.47, \pi/2)$

In 1775, Giovanni Fagnano stated a well-known problem in geometry: For a given acute triangle, what is the inscribed triangle with the smallest perimeter? By using a method based on calculus, Fagnano proved that the answer is the triangle whose vertices are at the base points of the altitudes of the given triangle, the so-called *altitude triangle* or *orthic triangle*. By construction, one can state the lemma [40]: *The orthic triangle is a 3-periodic* (P3) *billiard trajectory*. Now, within a given hexagon in the (ℓ, θ) family, one can trace two equilateral triangles by joining three nonconsecutive vertices with straight lines. It is easy to see that these two inscribed equilateral triangles have a common center, which is also the center of the C_3 symmetry of the hexagon. It follows that a P3 Fagnano orbit occurs when, from this center, one can reach three nonconsecutive sides of the hexagon with straight segments perpendicular to the sides, such as segments CO, CP, and CQ in Fig. 11(a). The solid red line [triangle OPQ in Fig. 11(a)] represents one such orbit in the ("right") hexagonal billiard with $\theta = \pi/2$ and $\ell = 0.47$. A continuous set of period-6 (P6) orbits parallel to the Fagnano orbit is also predicted. Two of them are shown in Fig. 11(b), one in red, the other in blue. The red solid line is a typical P6 orbit, where the two collision points on the sides are closer to the O, P, and Q points which define the center C in Fig. 11(a). The vertices of the hexagon impose a limit for the existence of such P6 orbits, as indicated by the solid blue line in Fig. 11(b). Segmented "bouncing ball" orbits are also allowed in the hexagons, such as the two-segment orbit represented by the solid red line in Fig. 11(c). Easy to see that the angle of incidence at the collision point P in Fig. 11(c) is $\pi/3$. Again, the vertices of the hexagon limit the subset of Ω where these orbits may occur. Finally, three-segment bouncing ball orbits are also known to exist in right triangles [40]. It may happen as well in the hexagons. The solid red lines in Fig. 11(d) show one such orbit. Here the angle of incidence is $\pi/3$ at point P and $\pi/6$ at point Q. Again, the blue line indicates the limit for these three-segment orbits. Notice that a single orbit is shown by the red lines in each case of Fig. 11. Within the region limited by the blue lines and the hexagon border, there are infinitely many such orbits. Also, rotations of $2\pi/3$ and $4\pi/3$ about the axis through the symmetry center in Figs. 11(c) and 11(d) generate

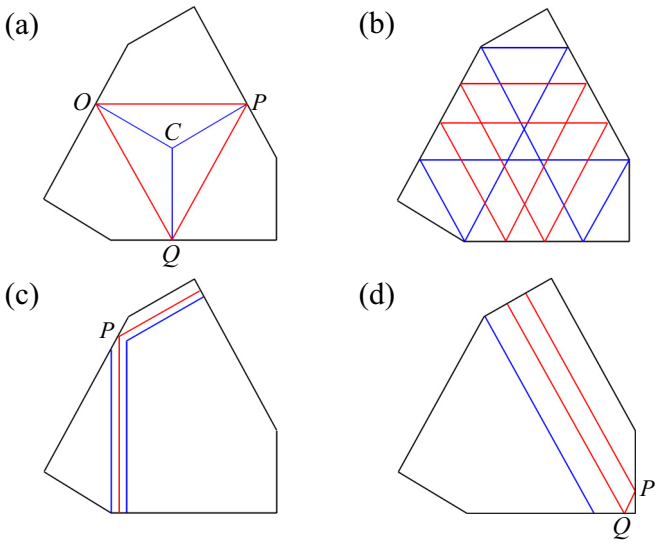

FIG. 11. Red (light gray, in the printed version) lines: Possible periodic orbits in the hexagon with $\ell = 0.47$ and $\theta = \pi/2$. (a) Period-3 Fagnano orbit, defined by the orthic triangle OPQ, centered at point C. (b) Period-6 orbit parallel to the Fagnano orbit in (a). (c) A two-segment bouncing ball orbit. (d) A three-segment bouncing ball orbit. The blue (dark gray, in the printed version) lines in (b), (c), and (d) indicate limits for the existence of the corresponding periodic orbits.

distinct triangular patterns, which are expected to show up in scarred quantum energy eigenfunctions. This expectation is confirmed by the density plots of the numerically calculated eigenfunctions shown in Fig. 12, in the right hexagon with $\ell = 0.47$. The solid yellow lines in Fig. 12 are exactly the periodic orbits described in Fig. 11, namely, Fagnano P3 in (a), parallel P6 in (b), two-segment bouncing ball in (c), and three-segment bouncing ball in (d). The scars are rather wide due to the many possible orbits parallel to the one shown in the figure. Calculated eigenvalues are given in the figure caption.

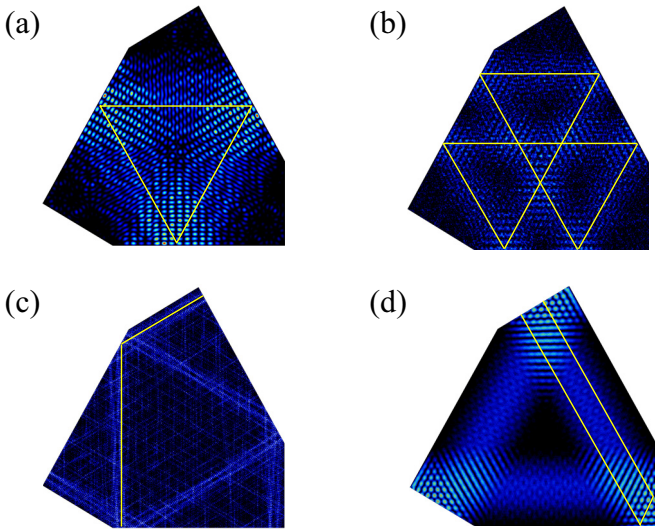

FIG. 12. Density plots of numerically calculated $|\varphi|^2$ in the right hexagonal billiard with $\ell = 0.47$, corresponding to eigenfunctions scarred by the classical periodic orbits described in Fig. 11, shown here by the yellow (white, in the printed version) lines. The calculated eigenvalues are $k^2 = 3.26305\ldots \times 10^4$ in (a), $3.90088\ldots \times 10^6$ in (b), $3.90237\ldots \times 10^6$ in (c) and $3.90545\ldots \times 10^6$ in (d).

B. Scarred energy eigenfunctions and Poincaré-Husimi representations in the FHB and SHB

Henceforth we focus our attention on the two representative hexagons studied in the previous sections, the FHB and the SHB. Notice that $\theta/(\pi/2) = 0.999952\ldots$ in the SHB, so that scarring around the periodic orbits just described in the neighboring right hexagon could be anticipated. We illustrate the persistence of the patterns of localized eigenstates with different energies through both eigenfunctions $\varphi_k(\vec{r})$ and their Poincaré-Husimi representation in a reduced phase space, briefly reviewed here. For a two-dimensional quantum system in the eigenstate $|\varphi_k\rangle$ with eigenfunction $\varphi_k(\vec{r}) = \langle\vec{r}|\varphi_k\rangle$, the Wigner function [41] is given by

$$W_k(\vec{r},\vec{p}) = \frac{1}{(2\pi\hbar)^2}\int \varphi_k(\vec{r}+\vec{s}/2)\varphi_k^*(\vec{r}-\vec{s}/2)e^{i\vec{p}\cdot\vec{s}/\hbar}\,d\vec{s}. \tag{16}$$

Integration of $W_k(\vec{r},\vec{p})$ over $\vec{p}$ gives the marginal distribution $|\langle\vec{r}|\varphi_k\rangle|^2$ and through a similar projection over $\vec{r}$ one obtains $|\langle\vec{p}|\varphi_k\rangle|^2$, the probability density in the momentum representation. Thus, the Wigner function might represent the quantum state of the system in the classical phase space swept by $\vec{r}$ and $\vec{p}$. However, as is well known, although $W_k(\vec{r},\vec{p})$ is real, it can take negative values in some regions of the phase space and, consequently, cannot be interpreted as a phase-space probability distribution. To circumvent this problem, Husimi [42] introduced a positive alternative, the Gaussian smoothing of the Wigner function

$$H_k(\vec{r},\vec{p}) = \int W_k(\vec{R},\vec{P})f(\vec{r},\vec{p};\vec{R},\vec{P})\,d\vec{R}\,d\vec{P}, \tag{17}$$

where

$$f(\vec{r},\vec{p};\vec{R},\vec{P}) = \frac{1}{(\pi\hbar)^2}e^{\left(-\frac{(\vec{r}-\vec{R})^2}{\delta^2}-\frac{(\vec{p}-\vec{P})^2}{(\hbar/\delta)^2}\right)} \tag{18}$$

and δ is a control parameter of the relative resolution of the distribution.

For the billiard system, it is convenient to use a Husimi representation on a Poincaré section, i.e., in a reduced phase space with Birkhoff coordinates (q, p). Let $\mathcal{L}$ be the length of the billiard perimeter. The classical dynamics is completely described by the bounce map defined in domain $\mathcal{D} = \{(q,p)\,|\,q \in [0,\mathcal{L}],\, p \in [-1,1]\}$ with invariant measure $d\mu = dqdp$. Now, for a given solution $\varphi_k(\vec{r})$ of the Helmholtz equation in Ω, with Dirichlet boundary conditions in $\partial\Omega$, the Poincaré-Husimi representation can be defined as [29,30,43]

$$h_k(q,p) = \left|\int_{\partial\Omega} c_k(q,p;s)u_k(s)\,ds\right|^2, \tag{19}$$

clearly positive definite, where

$$u_k(s) = \hat{n}\cdot\vec{\nabla}\varphi_k \tag{20}$$

is the normal derivative of φ_k on the boundary at position s, with $\hat{n}$ being the outward unit vector and

$$c_k(q,p;s) = C_k \sum_{m\in\mathbb{Z}} e^{ik[ap(s-q+m\mathcal{L})+\frac{b}{2}(s-q+m\mathcal{L})^2]} \tag{21}$$

is a one-dimensional coherent state obeying periodic boundary conditions on the billiard border. In units $\hbar = 1 = 2m$, $E_k = k^2$, the normalization constant $C_k = (k/\pi)^{1/4}$, $a = 1$ and $b = i$. We computed $h_k(q,p)$ for a number of localized states found in the hexagons, following the recipe in [29]. Given the C_3 symmetry in our polygons, we restrict the position to the relevant interval $0 \leqslant q \leqslant 1+\ell$, where the origin ($q = 0$) is taken at the left corner of the horizontal segment with unit length (see Fig. 1) and circulate the billiard counterclockwise, as usual. On the other hand, for the p-dependence of $h_k(q,p)$ we consider the full interval $-1 \leqslant p \leqslant 1$, so that the even parity $h_k(q,-p) = h_k(q,p)$, a signature of the time-reversal symmetry, could be observed. As usual, the Poincaré-Husimi functions are displayed in density plots with a gray scale, darker regions corresponding to higher function values. A host of distinct eigenfunctions $\varphi_k(\vec{r})$ and their Poincaré-Husimi representations $h_k(q,p)$ in the FHB and SHB are presented in the following. Notice that $k^2 \sim 10^4$ may correspond to a relatively low energy, as discussed later.

The plots in Fig. 13 are functions computed in the FHB ($|\varphi(\vec{r})|^2$ on the left, corresponding $h_k(q,p)$ on the right). The top left panel shows a scarred eigenfunction at $k^2 = 1.55454\ldots\times 10^3$, blurred by a set of a Fagnano P3 orbit (cyan solid line) at the center and parallel P6 orbits (such as the one shown by the yellow solid line), with collisions off the section in the interval $0.5 < q < 1$ with p distributed in the vicinity of ± 0.5. This localization phenomenon is represented by the broad two maxima in the Poincaré-Husimi function shown in the top right panel in Fig. 13. As mentioned above, the mirror symmetry with respect to $p = 0$ in $h_k(q,p)$ is due to the fact that the system is time-reversal-invariant. The middle panels in Fig. 13 show the situation for the singlet calculated at $k^2 = 2.09212\ldots\times 10^4$, in which scarring is due to P6 orbits only, such as the one represented by the yellow solid lines on the left panel. The bottom panels in Fig. 13 display the functions corresponding to the extended irregular state calculated at $k^2 = 2.01102\ldots\times 10^4$, which exhibits no characteristic feature of localization. Our Fig. 13 must be compared with Fig. 1 in [43], which reported similar calculations in non-polygonal billiards.

Fagnano P3 and parallel P6 orbits also scar the eigenfunction with $k^2 = 1.50545\ldots\times 10^3$ in the FHB shown in the left top panel in Fig. 14. Differently from the functions shown in Fig. 13, where collisions of the orbits off the boundary occur on the sides with unit length, here the specular reflections take place off the sides with length ℓ. The two broad maxima around $(q,p) = (1.25, \pm 0.5)$ in the Poincaré-Husimi representation on the top right panel in Fig. 14 connect the classical and quantum phenomena. The situation displayed in the bottom panels in Fig. 14 corresponds to the eigenmode with $k^2 = 3.19381\ldots\times 10^4$ in the SHB. Here collisions occur off the border on the segments with unit length with the 3-periodic and the 6-periodic orbits better resolved, as corroborated by the three maxima in the Poincaré-Husimi

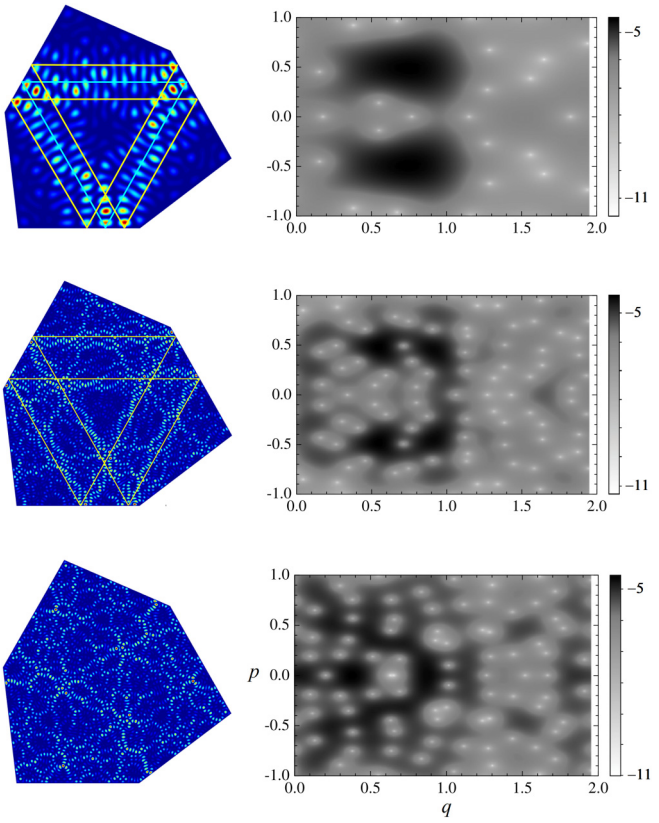

FIG. 13. Density plot of the numerically calculated $|\varphi|^2$ in the FHB (left panels) and corresponding decadic logarithm of the Husimi function $h(q,p)$ (right panels). The top panels correspond to a scarred state near Fagnano and P6 orbits, as indicated by the cyan and yellow lines, respectively, in the left panel. A higher-lying scarred eigenfunction near a P6 orbit is characterized in the middle panels. The bottom left panel shows the situation of an extended eigenfunction. From top to bottom, the calculated eigenvalues are, respectively, $k^2 = 1.55454\ldots\times 10^3$, $2.09212\ldots\times 10^4$, and $2.01102\ldots\times 10^4$.

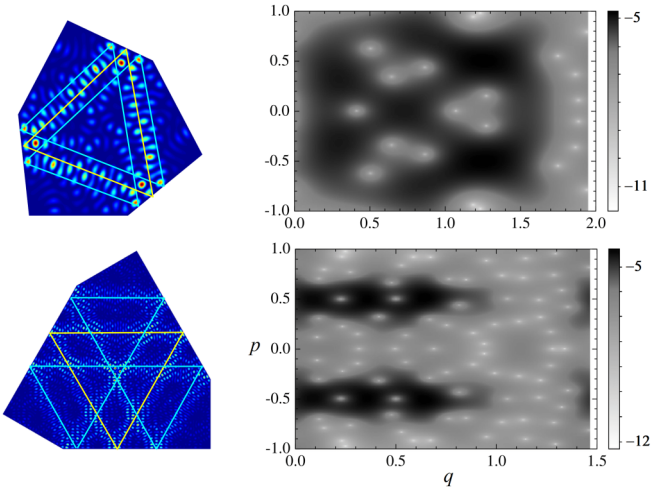

FIG. 14. Top left panel: Fagnano (yellow line) and P6 (cyan line) orbits and scarred $|\varphi|^2$ in the FHB, with $k^2 = 1.50545\ldots\times 10^3$, rotated with respect to the one shown in the top panel in Fig. 13. Bottom left panel: The same pattern in the SHB with $k^2 = 3.19381\ldots\times 10^4$. The right panels are the corresponding decadic logarithm of the Husimi functions.

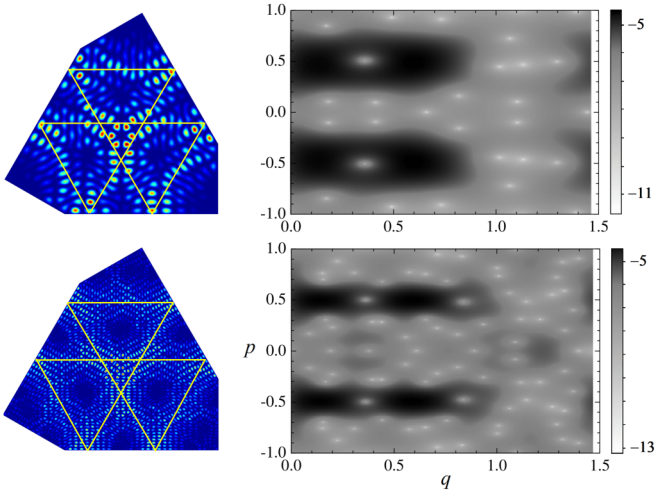

FIG. 15. Density plot of the numerically calculated $|\varphi|^2$ in the SHB (left panels), with eigenvalue $k^2 = 3.95919\ldots \times 10^3$ (top) and $k^2 = 3.05686\ldots \times 10^4$ (bottom), and corresponding decadic logarithm of the Poincaré-Husimi function $h_k(q, p)$ (right panels). Here both eigenstates exhibit the same pattern of an eigenfunction scarred solely by P6 orbits, without the central Fagnano one.

representation shown in the right bottom panel in Fig. 14, around $(q, p) = (0.1, \pm 0.5)$, $(0.37, \pm 0.5)$ and $(0.65, \pm 0.5)$. A repeated pattern of scarring by isolated P6 orbits in the SHB, without the presence of the central Fagnano P3 trajectory, is shown in Fig. 15, corresponding to $k^2 = 3.95919\ldots \times 10^3$ (top panels) and $k^2 = 3.05686\ldots \times 10^4$ (bottom panels).

Scarring by three-segment bouncing ball orbits with different patterns are shown in the SHB in Fig. 16, where $k^2 = 1.05369\ldots \times 10^4$ in the top plots and $k^2 = 3.10145\ldots \times 10^4$ in the bottom ones. The yellow and red solid lines are the orbits with collisions in the interval $0 < q < 1 + \ell$. In $0 < q < 1$ (horizontal segment of the border) in the top left panel, many three-segment orbits parallel to the one represented by the yellow line collide perpendicularly ($p = 0$) off the boundary

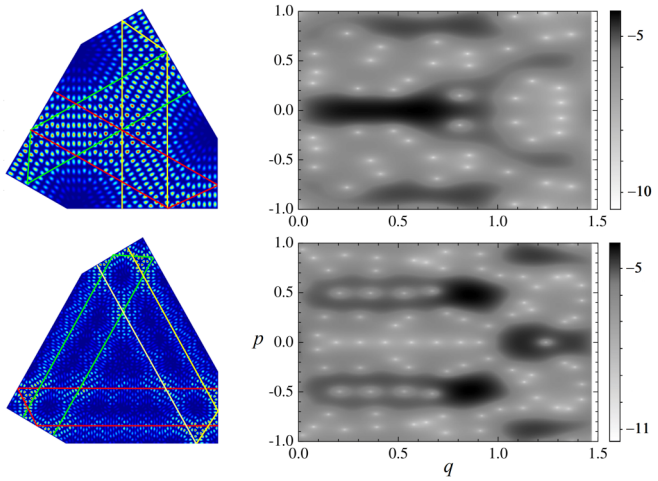

FIG. 16. The same as Fig. 15. Here the eigenfunctions are scarred around three-segment bouncing ball orbits (top, with $k^2 = 1.05369\ldots \times 10^4$; bottom, with $k^2 = 3.10145\ldots \times 10^4$). Three of such orbits are shown by the yellow, green, and red (gray, in the printed version) lines in each billiard.

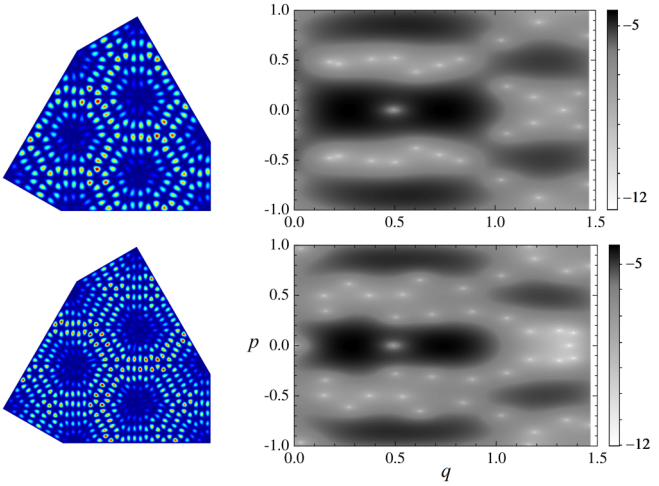

FIG. 17. The same as Fig. 15. Here the eigenfunctions are locked in the same lattice pattern with three complete hexagonal cells (dark regions) in Ω ($N_{\text{in}} = 3$). Other six incomplete cells ($N_{\text{out}} = 6$) appear near the vertices of the hexagon. The eigenvalues are $k^2 = 4.71001\ldots \times 10^3$ (top) and $k^2 = 8.49904\ldots \times 10^3$ (bottom).

around $q = 0.5$, whereas the red collisions occur in the vicinity of $q = 0.8$ with $p = \sin \pi/3 \approx 0.87$. In the interval $1 < q < 1 + \ell$, the collisions represented by the red line take place with the momenta distributed around $p = 0.5$. All these collisions are clearly represented by the maxima (dark regions) in the Poincaré-Husimi representation shown in the right top panel in Fig. 16. A similar situation is found in the bottom panels in Fig. 16, where a triangular pattern is observed in the eigenfunction (left bottom panel). Now, there is a single collision in $0 < q < 1$ around $q = 0.9$, and three in $1 < q < 1 + \ell$, two with $p = 0$, one around $q = 1.15$ the other around $q = 1.39$, and the third one with $p \approx 0.87$ around $q = 1.19$. Again, the calculated Poincaré-Husimi function shown in the bottom right panel in Fig. 16 clearly represents the scarring behavior just described.

C. Lattice states in the SHB

The proximity of the SHB to the right hexagon seems to favor the formation of standing waves patterns whose nodal regions are localized near lines that define hexagonal lattices within Ω, with a piecewise linear nodal line along $\partial\Omega$. The color code we use in the density plots is such that the central region of each lattice cell appears in dark blue, where $|\varphi(\vec{r})|^2 \approx 0$. Let N_{in} be the number of such regions which are fully displayed within Ω and N_{out} the number of dark cells which occur partially on the boundary $\partial\Omega$. In Fig. 17 we illustrate the case of the eigenmodes with $k^2 = 4.71001\ldots \times 10^3$ (top panels) and $k^2 = 8.49904 \times 10^3$ (bottom panels), for which $N_{\text{in}} = 3$ and $N_{\text{out}} = 6$. The squared eigenfunctions (left panels) clearly exhibit the same lattice pattern, a fact corroborated by the corresponding Poincaré-Husimi representations (right panels). The singlets in Fig. 18, for which $k^2 = 3.99736\ldots \times 10^3$ in the top panels and $k^2 = 8.33861\ldots \times 10^3$ in the bottom ones, show a similar situation. In this case, $N_{\text{in}} = 7$ and $N_{\text{out}} = 9$. The lattice states observed with $k^2 = 1.12581 \times 10^4$ and $k^2 = 3.08926 \times 10^4$

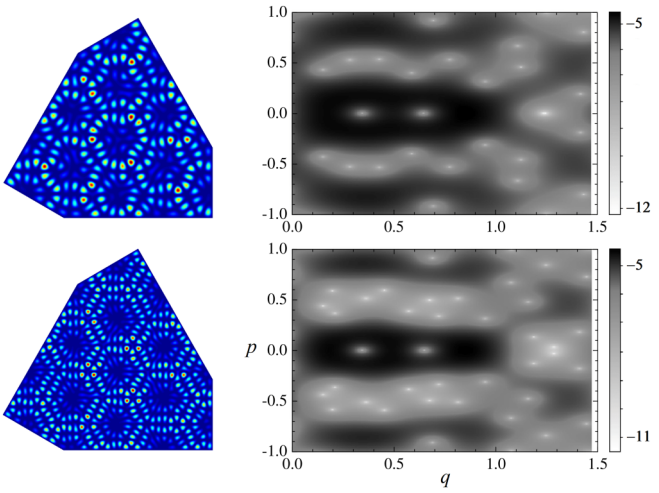

FIG. 18. The same as Fig. 17, with $N_{\text{in}} = 7$ and $N_{\text{out}} = 9$. The eigenvalues are $k^2 = 3.99736\ldots \times 10^3$ (top) and $k^2 = 8.33861\ldots \times 10^3$ (bottom).

shown, respectively, at the top and bottom panels in Fig. 19, have $N_{\text{in}} = 33$ and $N_{\text{out}} = 21$.

D. Focusing modes

The geometric properties of the Laplace operator in bounded Euclidean domains is, in fact, a long-standing subject. Recently, they have been reviewed by Grebenkov and Nguyen [44]. Here we draw our attention to the existence of the so called *focusing modes*, previously investigated in integrable domains with a curved border $\partial\Omega$. For Dirichlet boundary conditions, these are high-lying eigenstates localized at certain hot spots in Ω. A prototype geometry exhibiting such *high-frequency localization* is the billiard in a circle of radius R. In this case, separation of variables in polar coordinates (ρ, ϕ) leads to the exact solution

$$\varphi_{m,n}(\rho, \phi) \propto J_m(x_n \rho / R) \begin{bmatrix} \cos(m\phi) \\ \sin(m\phi) \end{bmatrix}, \tag{22}$$

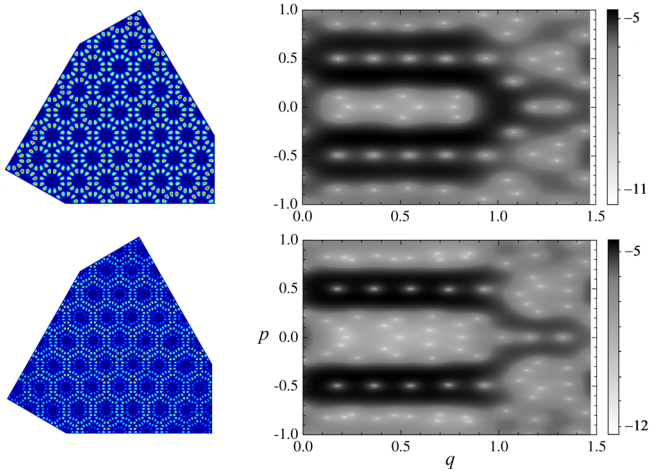

FIG. 19. The same as Figs. 17 and 18, with $N_{\text{in}} = 33$ and $N_{\text{out}} = 21$. The eigenvalues are $k^2 = 1.12581\ldots \times 10^4$ (top) and $k^2 = 3.08926\ldots \times 10^4$ (bottom).

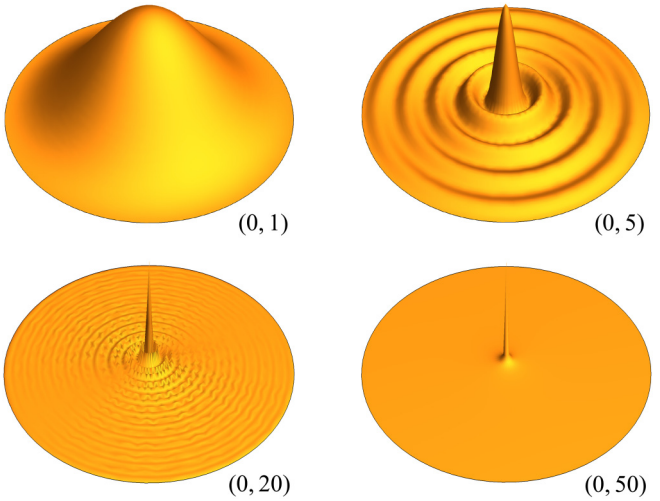

FIG. 20. Eigenfunctions of the circular billiard with quantum numbers (m, n), for $m = 0$ and $n = 1, 5, 20$ and 50. The panels were built with Zeleny's "Particle in an Infinite Circular Well" interface [45].

where m is a nonnegative integer and x_n is the zero of order n $(n = 1, 2, 3, \ldots)$ of the Bessel function $J_m(x)$. Thus, the ground state has quantum numbers $(m, n) = (0, 1)$ and exhibits a maximum at the center of the billiard with no nodal line in Ω. The ground-state eigenfunction of the circular billiard is shown in the top left panel in Fig. 20. By keeping $m = 0$, there are $(n - 1)$ concentric circular nodal lines between the center and the border of the billiard. The other three panels in Fig. 20 show the cases for $n = 5$, 20, and 50. Clearly, the larger the n, the larger is the degree of localization of the central peak. It is then pertinent to ask as to whether focusing modes might exist in polygonal billiards. They certainly do not occur in rectangles [44], but could they exist in more complex polygons, such as the hexagons investigated here? The symmetry center of the billiard is a candidate for such a hot spot. We sought numerical solutions with such a property in the hexagons and preliminary results, obtained with the finite element method, are reported in this subsection. The lower inset in Fig. 21 shows a perspective of the squared eigenfunction corresponding to the singlet with $k^2 = 2.87587\ldots \times 10^3$ in the SHB near the center, where it clearly displays a prominent peak. We conjecture that this eigenstate could play a role similar to the intermediate modes (0,5) or (0, 20) of the circle, towards an eventual high-frequency localized mode. Notice that in our calculation the center of the billiard is at the origin, i.e., $(x_c, y_c) = (0, 0)$. By fixing $y = y_c$ and varying x in the interval $-0.046 < x < 0.046$ we calculated the profile of the absolute value of the eigenfunction $|\varphi_y(x)|$ and the result is shown by the symbols in Fig. 21. The swept interval is indicated by the double-headed dashed white arrow in the lower inset. The solid red and blue lines are linear fits to the 10 leftmost and rightmost data points, respectively. In other words, the absolute value of the eigenfunction vanishes linearly as it reaches the first nodal line away from the billiard center. This behavior is shared with the high-frequency focusing mode shown in Fig. 20, as demonstrated in the upper inset of Fig. 21, where the solid black line is the radial profile of the central peak in the absolute value of the Bessel function

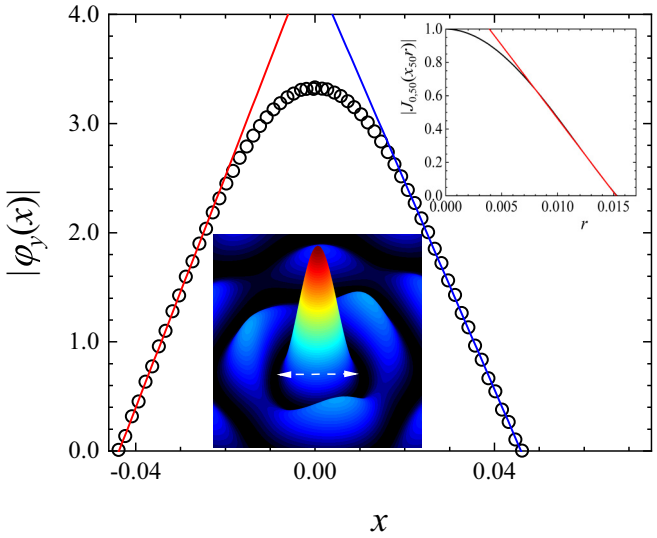

FIG. 21. Symbols: Calculated $|\varphi_y(x)|$ for the eigenstate with $k^2 = 2.87587 \times 10^3$ in the SHB, in the interval $-0.046 < x < 0.046$, for fixed $y = y_c = 0.0$ (origin at the billiard center). This interval is indicated by the horizontal double-headed dashed arrow in the lower inset, which shows a zoom of the central peak. Solid red and blue lines indicate that $|\varphi_y(x)|$ vanishes linearly with distance to the center. Upper inset: The same linear behavior is exhibited by the focusing mode (0,50) of the unit circle, shown in Fig. 20.

$J_0(x_{50}r)$. The red solid line is a linear fit to the asymptotic decay of $|J_0(x_{50}r)|$, just before it reaches the first nodal line at $r \approx 0.0152$. It is worth mentioning that this linear behavior in billiards is in contrast to the exponential decay of the localized eigenstates found in the Anderson model for a particle in a one-dimensional disordered potential [34].

E. Towards the deep semiclassical regime

The characterization of the semiclassical regime has always attracted a great deal of interest in the field of quantum chaos, as it is a major requirement for the application of random matrix theory (RMT). Purely quantum effects that might occur even at considerably high-lying eigenstates, such as dynamical localization and tunneling, may render the comparison with RMT inadequate [28–30,37]. In this subsection we report primary results of an ongoing investigation aimed at the observation persistent occurrence of localized modes in the SHB, as the presence of those modes without a classical counterpart might contribute for the poor agreement between the spectral data and the BR formulas for the nns discussed previously. For that purpose, the energy eigenstates are calculated with the VS method. Scarred states by three-segment and two-segment periodic orbits are displayed, respectively, in the top ($k^2 = 3.21213\ldots \times 10^5$) and bottom ($k^2 = 3.09734\ldots \times 10^6$) panels in Fig. 22. Representative trajectories are shown by the solid yellow, cyan, and red lines in the left panels. Notice that the situation in the top panels of Fig. 22 might be regarded as similar to the ones shown in Fig. 17, corresponding to lattice states with $N_{\text{in}} = 3$ and $N_{\text{out}} = 6$. The calculated Poincaré-Husimi function beautifully exhibits maxima corresponding to the three collisions in

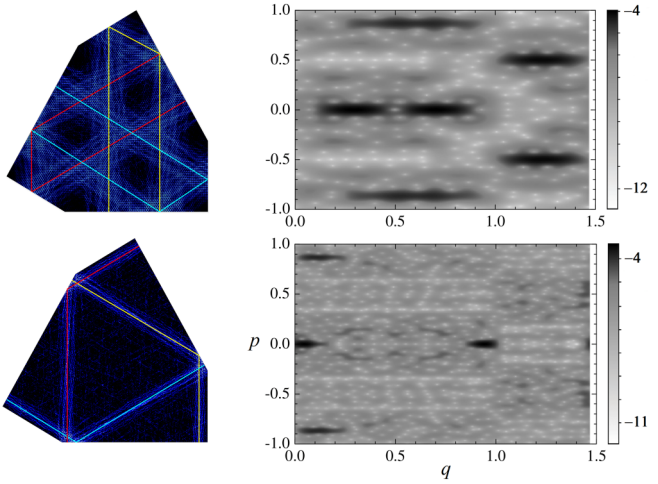

FIG. 22. High-lying eigenstates (left) and corresponding decadic logarithm of the Poincaré-Husimi representations (right) in the SHB, exhibiting a scar near three-segment bouncing ball orbits (top, with $k^2 = 3.21213\ldots \times 10^5$) and a scar near two-segment bouncing ball orbits (bottom, with $k^2 = 3.09734\ldots \times 10^6$).

$0 < q < 1$ (two with $p = 0$, one with $|p| \approx 0.87$) and the single collision in $1 < q < 1 + \ell$ (with $|p| = 0.5$). On the other hand, the situation depicted in the bottom panels in Fig. 22 is quite similar to the one shown in Fig. 12(c), found in the right hexagon. Again, the Poincaré-Husimi function connects the scarring phenomenon with the three collisions in $0 < q < 1$ (two with $p = 0$ near the corners, one with $|p| \approx 0.87$ near the leftmost corner) and no collisions in the $1 < q < 1 + \ell$ interval.

The top left panel in Fig. 23 shows the squared energy eigenfunction corresponding to energy eigenvalue $k^2 = 3.09679\ldots \times 10^6$. Scarring by P6 trajectories (cyan, red, and yellow solid lines) as well as by a set of three-segment bounc-

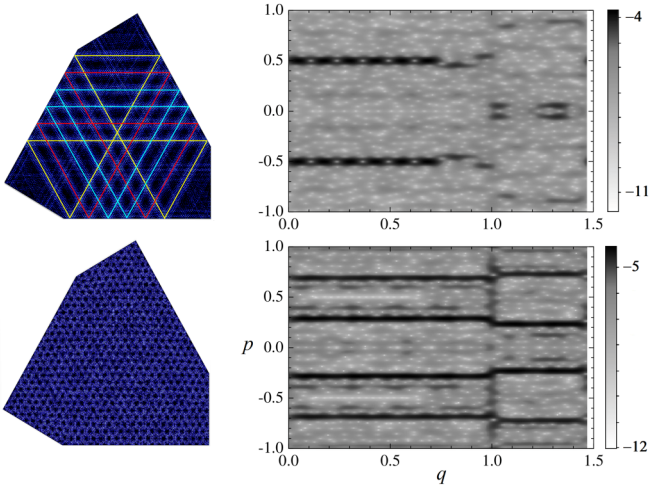

FIG. 23. High-lying eigenstates (left) and corresponding decadic logarithm of the Poincaré-Husimi representations (right) in the SHB, exhibiting a scar near three P6 orbits (top, with $k^2 = 3.09679\ldots \times 10^6$) and a higher-order lattice mode (bottom, with $k^2 = 3.09484\ldots \times 10^6$).

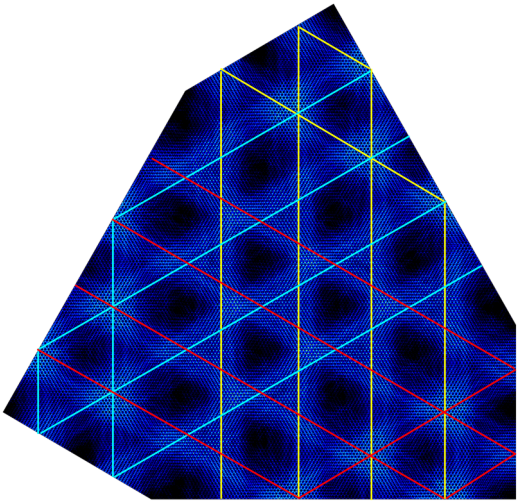

FIG. 24. Density plot of the numerically calculated $|\varphi|^2$ in the right hexagon exhibiting a lattice pattern which is associated with scars in the vicinity of six independent three-segment bouncing ball orbits, shown by yellow, cyan, and red solid lines. The calculated eigenvalue is $k^2 = 6.31914\ldots \times 10^5$.

ing ball orbits (not shown, for clarity) are present in this case. The six maxima in the corresponding Poincaré-Husimi representation in the interval $0 < q < 1$ around $p = 0.5$ reflect the collisions associated with the overwhelming signature of the three P6 orbits. The bottom panels in Fig. 23 display the functions corresponding to $k^2 = 3.09484\ldots \times 10^6$, a *superlattice* state with $N_{\rm in} = 498$ and $N_{\rm out} = 76$ whose Poincaré-Husimi representation exhibits a set of neighboring maxima around $|p| \approx 0.3$ and $|p| \approx 0.7$ in $0 < q < 1$ and around $|p| \approx 0.2$ and $|p| \approx 0.7$ in $1 < q < 1 + \ell$. The maxima are clearly not resolved from one another and appear as continuous dark horizontal stripes in the Poincaré-Husimi projection. As an addition to the rich gallery of localized eigenfunctions of the SHB system, Fig. 24 shows the state corresponding to $k^2 = 6.31914\ldots \times 10^5$ in the neighboring right billiard, an eigenfunction scarred by three-segment orbits such as the ones shown by the yellow, cyan, and red lines, bearing resemblance to a lattice state with $N_{\rm in} = 15$.

Upon completion of this work, we have not yet found a convincing focusing mode among the sorted high-lying eigenstates in the SHB. On the other hand, we have shown that at least some lattice modes might be related to scarred eigenstates, which are connected to periodic orbits in the classical limit. Thus, although we suspect that the numerous and persistent localized eigenstates found here do play a significative role in the determination of the deep semiclassical regime, the overall scenario thus far is not crystal clear. We still need to better characterize our spectra in that regard. An attempt based on the calculation of the ergodic parameter is presented in the next subsection.

F. Heisenberg and transport times

Quantum dynamical localization is a phenomenon that bears no relation to the eigenstates discussed in the previous subsections. Putting it briefly, it corresponds to a peculiar quantum distribution of the linear or angular momentum peaked at zero, with walls that decay exponentially, differently from the classical results, which predicts, for a chaotic or disordered system, a diffusive transport [37]. A review of the phenomenon can be found in Ref. [46]. An interesting feature of the quantum dynamical localization is that it allows us to estimate the conditions under which the comparison with the standard random matrix theory is adequate or, in other words, whether a given data set indeed belongs to the deep semiclassical regime. We follow closely Batistić and Robnik [30] in the short description below.

The key idea is to express the *ergodic parameter* $\alpha = t_H/t_T$, where t_H is the (quantum) Heisenberg time and t_T is the (classical) transport time, in terms of accessible magnitudes, such as the (quantum) energy E and the (classical) number of collisions off the billiard border, N_T. The Heisenberg time is $t_H = 2\pi\hbar\rho(E)$, where $\rho(E) = dN(E)/dE$ is the density of states. Here $N(E)$ is the number of levels below and up to energy E. For a particle of mass m in a billiard with area $\mathcal{A}$, the leading order of the Weyl formula gives

$$N(E) = \frac{m\mathcal{A}}{2\pi\hbar^2}E. \tag{23}$$

Thus, the Heisenberg time is

$$t_H = \frac{m\mathcal{A}}{\hbar}. \tag{24}$$

Now let $v = \sqrt{2E/m}$ be the speed of the particle at energy E and $\bar{\ell}$ the mean-free path. Then the transport time is given by

$$t_T = \frac{\bar{\ell}N_T}{v} = \frac{\bar{\ell}N_T}{\sqrt{2E/m}}. \tag{25}$$

If $\mathcal{P}$ is the length of the perimeter $\partial\Omega$, the Santaló's formula [47] $\bar{\ell} \approx \pi\mathcal{A}/\mathcal{P}$ leads to

$$\alpha = \frac{t_H}{t_T} = \frac{\mathcal{A}k}{N_T\bar{\ell}} = \frac{\mathcal{P}k}{\pi N_T}. \tag{26}$$

For our hexagons, $\mathcal{P} = 3(1 + \ell)$. The condition for the presence of quantum dynamical localization in a given energy spectrum, $\alpha \leqslant 1$, can then be written as

$$k \leqslant k_c = \frac{\pi N_T}{3(1+\ell)}. \tag{27}$$

The next step is to consider an ensemble of orbits initially directed perpendicularly to $\partial\Omega$ in the interval $0 < q < 1 + \ell$ and follow its random spreading as a function of the discrete time t. The symbols in Fig. 25 illustrate the results for the mean square momentum $\langle p^2\rangle$ as a function of $\log_{10} t$ (averaged in sets of 10^3 randomly chosen initial conditions) for the FHB and SHB systems. Saturation of $\langle p^2\rangle$ occurs at $t = N_T = 10^3$, for the FHB (black symbols) and at $N_T = 10^4$ for the SHB (red symbols). These numbers correspond to the critical values $k_c \approx 5.4 \times 10^2$ for the FHB, and $k_c \approx 7.1 \times 10^3$, for the SHB. On the other hand, our calculations of the nns distribution of singlets, for instance, correspond to spectra starting at $k_{\rm min}$ and ending at $k_{\rm max}$, with $(k_{\rm min}, k_{\rm max}) = (1.3 \times 10^3, 1.4 \times 10^3)$ in the FHB and $(1.7 \times 10^3, 1.9 \times 10^3)$ in the SHB. Our estimate gives $k_c < k_{\rm min}$ in the FHB, thus indicating that the investigated spectrum is fully within the deep semiclassical regime in that billiard. For the SHB, we have $k_c > k_{\rm max}$, clearly indicating the semiclassical regime has not

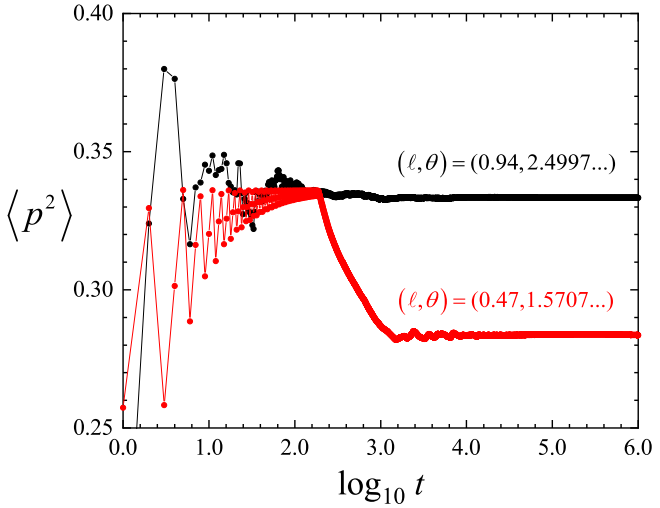

FIG. 25. Calculated mean square of the momentum as a function of the logarithm of the discrete time t (number of collisions of the particle off the billiard boundary). Black [red (gray, in the printed version)] solid circles are data for the FHB (SHB). Lines are guides for the eyes.

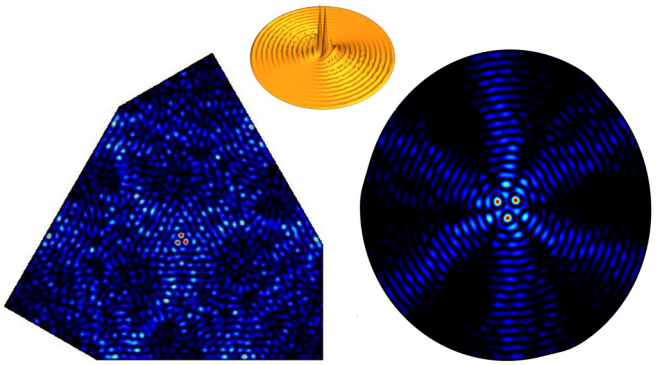

FIG. 26. Left panel: Density plot of $|\varphi|^2$ in the SHB corresponding to eigenvalue $k^2 = 1.2952\ldots \times 10^4$. Besides the broad scar due to parallel P6 orbits, this mode exhibits three pronounced peaks near the billiard center, bearing resemblance to the higher-order focusing mode of the C3S-D shown in the right panel and the (1,15) mode of the circle in the inset, built with Zeleny's "Particle in an Infinite Circular Well" interface [45].

been reached. The overall results are consistent with the spectral statistics discussed in the previous section, namely, the agreement with the GOE and GUE results for the singlets and doublets in the *fast* billiards, and with adequate intermediate formulas for the *slow* ones.

V. CONCLUSIONS

In summary, a family of biparametric time-reversal-invariant billiards with the additional C_3 point symmetry has been introduced and thoroughly investigated in numerical experiments. Calculations of the relative measure in a reduced phase space, as well as the decay of the position autocorrelation function, allowed us to identify hexagons with a *strong* mixing character, as a numerical conjecture. Prior to this work, to our knowledge, *irrational* triangles [15,16] were the only billiards in polygons, which are never chaotic, to exhibit numerical evidence for this ergodic property. On the other hand, there are rigorous mathematical theorems supporting the *weakly* mixing property in polygonal billiards for the *rational* case only, i.e., when all angles are rational with π [48]. The difficult class of irrational billiards still lacks rigorous results. Pertinent discussions may be found in Refs. [49–52]. As far as the quantum properties are concerned, the results reported here are the following: (1) Evidence was found that the C_3-symmetric irregular hexagons with the classical strong mixing property (fast decay of correlations) exhibit the anomalous nearest neighbor spacing distribution predicted by Leyvraz, Schmit, and Seligman for chaotic domains, namely, singlets or doublets follow the GOE or GUE, respectively, result of random matrix theory. (2) For the intermediate cases, we successfully used fitting formulas previously introduced by Brody [$p_{\mathrm{B}}(s)$], Berry and Robnik [$p_{\mathrm{BR}}(s)$], and Batistić and Robnik [$p_{\mathrm{BRB}}(s)$], for both singlets and doublets, for the first time in the case of doublets. (3) Energy eigenfunctions have been investigated in the general context of localization in the hexagons. Numerous eigenmodes and corresponding Poincaré-Husimi representations in a phase space with Birkhoff coordinates (q, p) have been reported, including scarred eigenfunctions and lattice modes, as well as evidence for focusing modes (high-frequency localization). (4) Finally, estimates of the ergodic parameter, the ratio between the Heisenberg time and the classical, diffusive-like, transport time, support the formulas we used to fit the nns distributions in a given spectrum, both in the hexagonal family and in C_3-symmetric billiards with a smooth boundary. The hexagonal billiards offer further opportunities for theoretical and numerical studies. For instance, the presence of focusing modes in high-lying states was not observed yet. Additional evidence of such a trend toward a high-frequency localization in the SHB is shown here in the left panel of Fig. 26, where a density plot of $|\varphi|^2$ corresponding to eigenvalue $k^2 = 1.2952\ldots \times 10^4$ is presented. Besides the ghost of P6 orbits, this mode exhibits three pronounced peaks in the vicinity of the billiard center. This might be associated with a higher-order focusing mode, such as the eigenmode of the circle with quantum numbers (1,15) shown in the inset in Fig. 26, which has two pronounced peaks near the center, or the eigenmode of the C3S-D billiard shown in the right panel in Fig. 26, also with three pronounced peaks near the center. In addition, the interesting and challenging phenomenon of superscars [39] in irrational polygons must also be investigated in the foreseeing future. It is most likely, periodic orbit channels, such as those shown in the top left panel in Fig. 23, and strong diffraction are present in the hexagons. It is also worth mentioning that the vast subject of nodal portraits [53] was not investigated here. Finally, there is certainly room for experimental research in *open* C_3-symmetric hexagons, and we would like to stress that microwave scattering experiments [54] in flat hexagonal resonators are under way.

ACKNOWLEDGMENTS

Useful discussions with Prof. L. Kaplan are gratefully acknowledged. This work has been supported by the Brazilian Agencies CNPq, CAPES, and FACEPE.

[1] M. L. Mehta, *Random Matrices* (Elsevier, Amsterdam, 2004).
[2] M. V. Berry and M. Tabor, Proc. R. Soc. London A **356**, 375 (1977).
[3] O. Bohigas, M. J. Giannoni, and C. Schmit, Phys. Rev. Lett. **52**, 1 (1984).
[4] D. Ullmo, Scholarpedia **11**, 31721 (2016).
[5] N. Chernov and R. Markarian, *Chaotic Billiards*, Mathematical Surveys and Monographs Vol. 127 (American Mathematical Society, Providence, RI, 2006).
[6] F. Leyvraz, C. Schmit, and T. H. Seligman, J. Phys. A: Math. Gen. **29**, L575 (1996).
[7] B. Dietz, T. Klaus, M. Miski-Oglu, A. Richter, and M. Wunderle, Phys. Rev. Lett. **123**, 174101 (2019).
[8] J. P. Keating and J. M. Robbins, J. Phys. A: Math. Gen. **30**, L177 (1997).
[9] C. Dembowski, H.-D. Gräf, A. Heine, H. Rehfeld, A. Richter, and C. Schmit, Phys. Rev. E **62**, R4516 (2000).
[10] R. Schäfer, M. Barth, F. Leyvraz, M. Müller, T. H. Seligman, and H.-J. Stöckmann, Phys. Rev. E **66**, 016202 (2002).
[11] C. Dembowski, B. Dietz, H.-D. Gräf, A. Heine, F. Leyvraz, M. Miski-Oglu, A. Richter, and T. H. Seligman, Phys. Rev. Lett. **90**, 014102 (2003).
[12] B. Dietz, A. Heine, V. Heuveline, and A. Richter, Phys. Rev. E **71**, 026703 (2005).
[13] A. Gusso, M. G. E. da Luz, and L. G. C. Rego, Phys. Rev. B **73**, 035436 (2006).
[14] T. Araújo Lima and R. B. do Carmo (unpublished).
[15] T. Araújo Lima, S. Rodríguez-Pérez, and F. M. de Aguiar, Phys. Rev. E **87**, 062902 (2013).
[16] G. Casati and T. Prosen, Phys. Rev. Lett. **83**, 4729 (1999).
[17] M. Robnik, J. Dobnikar, A. Rapisarda, T. Prosen, and M. Petkovsek, J. Phys. A **30**, L803 (1997).
[18] P. J. Richens and M. V. Berry, Physica D **2**, 495 (1981).
[19] D. D. de Menezes, M. Jar e Silva, and F. M. de Aguiar, Chaos **17**, 023116 (2007).
[20] E. Vergini and M. Saraceno, Phys. Rev. E **52**, 2204 (1995).
[21] A. H. Barnett and T. Betcke, Chaos **17**, 043125 (2007).
[22] T. A. Brody, Lett. Nuovo Cimento **7**, 482 (1973).
[23] M. V. Berry and M. Robnik, J. Phys. A **38**, 2413 (1984).
[24] F. Izrailev, Phys. Rep. **196**, 299 (1990).
[25] S. Schierenberg, F. Bruckmann, and T. Wettig, Phys. Rev. E **85**, 061130 (2012).
[26] B. Batistić, C. Lozej, and M. Robnik, Phys. Rev. E **100**, 062208 (2019).
[27] T. Prosen and M. Robnik, J. Phys. A: Math. Gen. **32**, 1863 (1999).
[28] B. Batistić and M. Robnik, J. Phys. A: Math. Theor. **43**, 215101 (2010).
[29] B. Batistić and M. Robnik, J. Phys. A: Math. Theor. **46**, 315102 (2013).
[30] B. Batistić and M. Robnik, Phys. Rev. E **88**, 052913 (2013).
[31] M. V. Berry and S. Klein, Eur. J. Phys. **18**, 222 (1997).
[32] F. Haake, *Quantum Signatures of Chaos*, 2nd ed. (Springer, New York, 2004).
[33] A. Lagendijk, B. van Tiggelen, and D. S. Wiersma, Phys. Today **62**(8), 24 (2009).
[34] S. Wimberger, *Nonlinear Dynamics and Quantum Chaos, An Introduction*, Graduate Texts in Physics (Springer, New York, 2014).
[35] C. Lozej, D. Lukman, and M. Robnik, Phys. Rev. E **103**, 012204 (2021).
[36] E. J. Heller, Phys. Rev. Lett. **53**, 1515 (1984).
[37] F. Borgonovi, G. Casati, and B. Li, Phys. Rev. Lett. **77**, 4744 (1996).
[38] E. Bogomolny and C. Schmit, Phys. Rev. Lett. **92**, 244102 (2004).
[39] E. Bogomolny, J. Phys. Commun. **5**, 055010 (2021).
[40] S. Tabachnikov, *Geometry and Billiards*, Student Mathematical Library Vol. 30 (American Mathematical Society, Providence, RI, 2005).
[41] E. P. Wigner, Phys. Rev. **40**, 749 (1932).
[42] K. Husimi, Proc. Phys. Math. Soc. Jpn. **22**, 264 (1940).
[43] A. Bäcker, S. Fürstberger, and R. Schubert, Phys. Rev. E **70**, 036204 (2004).
[44] D. S. Grebenkov and B.-T. Nguyen, SIAM Rev. **55**, 601 (2013).
[45] E. Zeleny, Particle in an infinite circular well, http://demonstrations.wolfram.com.
[46] T. Prosen, in *Proceedings of the International School of Physics*, edited by G. Casati, I. Guarneri, and U. Smilansky (IOS Press, Amsterdam, 2000), p. 473.
[47] L. A. Santaló and M. Kac, *Integral Geometry and Geometric Probability* (Cambridge University Press, Cambridge, 2004).
[48] A. M. Sabogal and S. Troubetzkoy, Bull. London Math. Soc. **49**, 141 (2017).
[49] J. Wang, G. Casati, and T. Prosen, Phys. Rev. E **89**, 042918 (2014).
[50] E. Gutkin, J. Stat. Phys. **83**, 7 (1996).
[51] E. Gutkin, Chaos **22**, 026116 (2012).
[52] G. W. Tokarsky, Commun. Math. Phys. **335**, 1211 (2015).
[53] S. R. Jain and R. Samajdar, Rev. Mod. Phys. **89**, 045005 (2017).
[54] R. B. do Carmo and F. M. de Aguiar, Sci. Rep. **9**, 3634 (2019).